



DIPLOMARBEIT

Ordered structures formed by ultrasoft, anisometric particles

Ausgeführt am Institut für

Theoretische Physik
der Technischen Universität Wien

unter der Anleitung von

Ao. Univ. Prof. Dr. Gerhard Kahl
Institut für Theoretische Physik (E136)
Technische Universität Wien

durch

Markus Weißenhofer
Gartenstraße 4, 4482 Ennsdorf

Wien, October 24, 2017

(Markus Weißenhofer)

Abstract

In this thesis a classical density functional theory approach was implemented in order to describe the formation of ordered structures of ultrasoft, anisometric particles. Using a mean-field ansatz for the functional, the single-particle density, which is assumed to be periodic and to be defined within a single unit cell, is obtained in an unrestricted optimization of this functional with respect to the density profile. For the optimization, a preconditioned conjugate gradient algorithm was implemented, which allows for a simultaneous minimization of the free energy with respect to the density profile and the lattice vectors. This numerical approach was used to study the impact of anisometry on the thermodynamic properties and the structures of an ultrasoft model system.

Contents

1	Introduction and Motivation	4
1.1	Microphases in Soft Matter Physics	4
1.2	Anisotropy-Driven Self Assembly	5
1.3	Scope and Organization of this Thesis	6
1.4	Acknowledgements	7
2	Theoretical Background	8
2.1	Classical Density Functional Theory	8
2.2	The Mean Field Functional	12
2.3	The System	16
2.4	Shape and Orientation Analysis of the Single-particle Density Profile	21
3	Minimization Method	24
3.1	Basic Assumptions for the Density Profile	24
3.2	Deriving a Numerically Treatable Expression for the Functional	26
3.3	Minimization Algorithm	27
3.4	The Spherical GEM-4 Model	30
4	Results	34
4.1	Introducing Anisotropy into the GEM-4 model	34
4.2	Stable and Metastable Microphases of the modified GEM-4 Model	41
4.3	Cluster Crystals Formed by a Modified GEM-4 Model	48

5	Conclusion & Outlook	60
A	Details of the Minimization Algorithm	62
A.1	Minimizing the functional with respect to the density profile .	62
A.2	Minimizing with respect to the lattice parameters	64
B	Summation over the Reciprocal Lattice	67

Chapter 1

Introduction and Motivation

1.1 Microphases in Soft Matter Physics

The occurrence of microphases in complex fluids, i.e. ordered structures that are in their length scale intermediate between the microscopic and the macroscopic length scale, is a topic that has attracted considerable attention in recent years [1–16]. Microphases are characterized by an inhomogeneous density with periodic modulations, which, although being much larger than the particles, cannot be considered macroscopic [11].

For example, microphases are present in solutions of amphiphilic molecules in a solvent consisting of polar and apolar species [17]. In these systems, the hydrophilic and the hydrophobic parts of the molecules tend to segregate in two separate domains, which is prevented by the intramolecular bond within the amphiphilic molecules. The competition between these tendencies can lead to the formation of clusters, which then occur in one, two or three spatial directions.

A similar mechanism can be found in fluids consisting of hard-core spherical colloids with attractive behaviour in short range and repulsive in long-range. While particle aggregation is favoured by the short-range attraction, it is suppressed by the long-range repulsion, leading to the formation of microphases in two and three dimensions [5–10].

An alternative type of systems which features the occurrence of microphases

are systems whose constituents interact via a purely repulsive, ultrasoft potential. Ultrasoft means that the interaction is bounded, allowing particles to fully overlap with an energy penalty. Bounded interactions occur as effective potentials [18] between polymers [19–21], dendrimers [22, 23], microgels [24–26] or coarse-grained block copolymers [27, 28]. The conditions under which ultrasoft interactions lead to clustering have been conjectured by Likos et al. [29] and were explicitly confirmed by computer simulations by Mladek et al. [15]. Irrespective of the specific nature of the interaction, the tendency of one-component systems to form clusters rests upon the behaviour of the Fourier transform of the interaction: if the Fourier transform of the potential has a negative minimum at some wave vector $\mathbf{q} \neq 0$, density modulations with a characteristic length $d \sim 2\pi/|\mathbf{q}|$ are preferred over the other Fourier components of the single-particle density [11]. Furthermore, this feature gives rise to the fact, that there is a single length-scale for the lattice constants which is almost unchanged when changing the density of the crystal [14].

The theoretical description of the formation of microphases can be achieved via Simulations (Monte Carlo (see for instance [30]) and molecular dynamics (see for instance [31])) which are numerically expensive and thus very time consuming and via classical density functional theory (DFT) [32]. The framework of classical DFT allows for the computation of thermodynamic properties (free energy, phase transitions) and correlation functions via a variational principle.

1.2 Anisometry-Driven Self Assembly

Anisometry in the inter-particle potential is a key feature to trigger self assembly. Due to advances in synthetic colloidal chemistry, the interactions can now be tailored specifically, either by controlling the shape of the particles or by decoration of the surface, in order to obtain desired target structures (for an overview of the state-of-the-art techniques in colloidal synthesis see for instance [33] and [34]).

It is evident, that the shape of a particle has a substantial impact on the formation of microphases, which is best illustrated by considering hard particles in a box where the maximum of the packing fraction depends strongly on the shape: for hard spheres this maximum is at 0.74 (which corresponds to a face-centered cubic lattice), whereas for hard cubes it is at 1.0.

A typical example where the phase behaviour is dominated by the shape of the particles are suspensions of rigid rods. They were first described by Onsager [35] within a simple mean-field theory and have been studied extensively by experiments [36] and simulations [37] ever since. Rigid rods show a rich phase behaviour including a smectic, a nematic and a liquid phase.

If colloidal particles are suspended in a dilute solution of depletants (e.g. non-adsorbing polymers, nanoparticles, micelles [38]) depletion forces (first described by Asakura and Oosawa [39]) arise which are very sensitive to changes of the shape of the colloids. This has been shown by Rossi et al. [40] who studied the behaviour of silica cubes in various aqueous solutions of non-adsorbing polymers. Here, the phase behaviour depends on the roundness of the cubes' edges, which defines the size of the interstices, and the size of the dissolved polymer. In Ref. [41] depletion forces were used to bind complementary colloids using a lock and key mechanism.

A different way to engineer anisometric interactions is by decorating the surface of the particles with "sticky patches" [42]. As a prominent example, "triblock Janus" particles (spherical colloids with electrostatic repulsion in the middle and hydrophobic attraction at the poles) were tailored to form a kagome lattice [43]. In a similar manner, "Janus matchsticks" were prepared which combine shape and surface anisometry and allow for the formation of multipod structures [44].

1.3 Scope and Organization of this Thesis

For this thesis, an unconstrained density functional theory approach to microphase formation of ultrasoft, anisometric particles has been developed. To

verify its correctness, results of this approach are compared with reference data available for spherical particles.

The approach is then extended to anisometric particles. In Sec. 4.1 the impact of an increasing anisometry in the potential on the emerging density profiles and lattices is presented. The structural and thermodynamic properties of a system interacting via a fixed anisometric potential are presented in Sections 4.2 and 4.3.

The details of the minimization algorithm are found in Appendix A. Appendix B contains additional information on the convergence of the algorithm.

1.4 Acknowledgements

I would like to express my sincerest gratitude to Prof. Gerhard Kahl who supported me throughout the thesis in a highly proficient and friendly manner and who gave me the possibility to present the results obtained within my thesis at the Density Functional Days in Tübingen. Furthermore I would like to thank Dr. Davide Pini who was very eager to introduce me to his approach and to share his experiences.

Also, I would like to thank the TU Wien as well as the CMS for generous financial support. I am also thankful for the computing resources at the VSC-3 provided by the Vienna Scientific Cluster.

I would also like to thank (in alphabetical order) Benedikt Hartl, Clemens Jochum, Gernot Kern, Michael Obermann, Sandra Preinknoll, Klaus Steiner, David Toneian and Susanne Wagner for their support.

Chapter 2

Theoretical Background

The first section of this chapter gives an introduction to the concept of the classical density functional theory (DFT) which *”provides an ideal microscopic theory to address freezing and crystallization problems”* ([45], p. 1). In the second section, the mean field functional, which represents the basis for all the calculations, is derived and its range of applicability is discussed. The third section focuses on the anisotropic pair potential that has been considered in this thesis. In the closing section of this chapter, two useful tools which are important for comparing the density profiles are introduced.

2.1 Classical Density Functional Theory

This section heavily borrows from the book of J. P. Hansen and I. R. McDonald [46]. The theoretical basis for the classical DFT is formed by the Hohenberg-Kohn-Mermin theorems, which will be proven below. Beforehand some definitions which are relevant in the following are recalled. The Hamiltonian \mathcal{H} for a system consisting of N particles is given by

$$\mathcal{H}_N(\mathbf{r}^N, \mathbf{p}^N) = K_N(\mathbf{p}^N) + V_N(\mathbf{r}^N) + V_{\text{ext}}(\mathbf{r}^N) \quad (2.1.1)$$

where $K_N(\mathbf{p}^N)$ is the kinetic energy, $V_N(\mathbf{r}^N)$ is the interaction potential between the particles and $V_{\text{ext}}(\mathbf{r}^N)$ is the external potential. \mathcal{H} is a function of the $3N$ coordinates $\mathbf{r}^N = (\mathbf{r}_1, \dots, \mathbf{r}_N)$ and the $3N$ momenta $\mathbf{p}^N = (\mathbf{p}_1, \dots, \mathbf{p}_N)$

of the particles.

The following calculations are performed within the framework of the grand canonical ensemble which is an ensemble of systems with the same chemical potential μ , temperature T and volume V . The equilibrium phase space probability density for this ensemble is given by

$$f_0(\mathbf{r}^N, \mathbf{p}^N; N) = \frac{1}{\Xi} \exp[-\beta(\mathcal{H} - N\mu)] \quad (2.1.2)$$

where Ξ denotes the grand partition function. It is useful to introduce the following definition for the trace in the grand canonical ensemble

$$\text{Tr}[\dots] = \sum_{N=0}^{\infty} \frac{1}{h^{3N} N!} \int \int [\dots] d\mathbf{r}^N d\mathbf{p}^N \quad . \quad (2.1.3)$$

By this definition Ξ can be written as

$$\Xi = \text{Tr}[\exp[-\beta(\mathcal{H} - N\mu)]] \quad . \quad (2.1.4)$$

One can easily verify that $\text{Tr}[f_0] = 1$ by inserting Eq. (2.1.2) into Eq. (2.1.3) (in the following the arguments of f_0 are dropped for simplicity). The link between the grand canonical ensemble and the grand potential Ω is established via the relation

$$\Omega = -k_B T \ln \Xi \quad (2.1.5)$$

where k_B denotes the Boltzmann constant. The grand potential Ω and the free energy F are connected via the Legendre transformation

$$\Omega = F - N\mu \quad . \quad (2.1.6)$$

The microscopic single-particle density $\rho(\mathbf{r})$ is given by a sum of Dirac delta functions

$$\rho(\mathbf{r}) = \sum_{n=1}^N \delta(\mathbf{r} - \mathbf{r}_n) \quad (2.1.7)$$

and its equilibrium ensemble average, the equilibrium single-particle density $\rho_0^{(1)}(\mathbf{r})$, by the relation

$$\rho_0^{(1)}(\mathbf{r}) = \text{Tr}[f_0 \rho(\mathbf{r})] \quad . \quad (2.1.8)$$

In the following, it is useful to split the free energy F into an external part and an intrinsic part \mathcal{F}

$$F = \mathcal{F} + \int d\mathbf{r} \rho_0^{(1)}(\mathbf{r}) V_{\text{ext}}(\mathbf{r}) \quad . \quad (2.1.9)$$

Lemma. *Let $f(\mathbf{r}^N, \mathbf{p}^N)$ be a phase space probability density with $f(\mathbf{r}^N, \mathbf{p}^N) \geq 0 \forall (\mathbf{r}^N, \mathbf{p}^N)$ and $\text{Tr}[f] = 1$ and let the functional $\Omega[f]$ be defined as*

$$\Omega[f] = \text{Tr}[f(\mathcal{H} - N\mu + k_B T \ln f)] \quad . \quad (2.1.10)$$

Then

$$\Omega[f] \geq \Omega[f_0] \quad . \quad (2.1.11)$$

Proof. Inserting Eq. (2.1.2) into Eq. (2.1.10) yields

$$\Omega[f_0] = \text{Tr}[f_0(\mathcal{H} - N\mu - k_B T \ln \Xi - \mathcal{H} + N\mu)] = -k_B T \ln \Xi = \Omega \quad . \quad (2.1.12)$$

Therefore

$$\begin{aligned} \Omega[f] - \Omega[f_0] &= k_B T [\text{Tr}[f \ln f] - \text{Tr}[f \ln f_0]] \\ &= k_B T \text{Tr}[f_0((f/f_0) \ln(f/f_0) - (f/f_0) + 1)] \quad . \end{aligned} \quad (2.1.13)$$

The argument of the trace is non-negative for any point in phase space since $x \ln x \geq x - 1$ for $x > 0$. The inequality (2.1.11) is thereby verified.

Theorem 1. *For given V_N , T and μ the intrinsic free energy functional*

$$\mathcal{F}[\rho_0^{(1)}] = \text{Tr}[f_0(K_N + V_N + k_B T \ln f_0)] \quad (2.1.14)$$

is a unique functional of the equilibrium single-particle density $\rho_0^{(1)}(\mathbf{r})$.

Proof. f_0 for given V_N , T and μ only depends on the external potential $V_{\text{ext}}(\mathbf{r})$. Eq. (2.1.8) implies that the same is true for $\rho_0^{(1)}(\mathbf{r})$. Let us assume

that there exists a different external potential $V'_{\text{ext}}(\mathbf{r})$ that leads to the same $\rho_0^{(1)}(\mathbf{r})$. This different external potential results in a different Hamiltonian $\mathcal{H}' = K_N + V_N + V'_{\text{ext}}$ with a corresponding equilibrium phase space density f'_0 . The inequality (2.1.11) implies that

$$\begin{aligned}\Omega' &= \text{Tr}[f'_0(\mathcal{H}' - N\mu + k_B T \ln f'_0)] < \text{Tr}[f_0(\mathcal{H}' - N\mu + k_B T \ln f_0)] \\ &= \Omega + \text{Tr}[f_0(V'_{\text{ext}} - V_{\text{ext}})] \quad . \quad (2.1.15)\end{aligned}$$

The last term can be simplified by the following analytical transformation

$$\begin{aligned}\text{Tr}[f_0(V'_{\text{ext}} - V_{\text{ext}})] &= \text{Tr} \left[\int d\mathbf{r} f_0 \rho(\mathbf{r})(V'_{\text{ext}}(\mathbf{r}) - V_{\text{ext}}(\mathbf{r})) \right] \\ &= \int d\mathbf{r} \text{Tr}[f_0 \rho(\mathbf{r})](V'_{\text{ext}}(\mathbf{r}) - V_{\text{ext}}(\mathbf{r})) \quad (2.1.16) \\ &= \int d\mathbf{r} \rho_0^{(1)}(\mathbf{r})(V'_{\text{ext}}(\mathbf{r}) - V_{\text{ext}}(\mathbf{r})) \quad .\end{aligned}$$

Thus the inequality (2.1.15) can be written as

$$\Omega' < \Omega + \int \rho_0^{(1)}(\mathbf{r})(V'_{\text{ext}}(\mathbf{r}) - V_{\text{ext}}(\mathbf{r}))d\mathbf{r} \quad . \quad (2.1.17)$$

Interchanging the primed and the unprimed quantities yields

$$\Omega < \Omega' + \int \rho_0^{(1)}(\mathbf{r})(V_{\text{ext}}(\mathbf{r}) - V'_{\text{ext}}(\mathbf{r}))d\mathbf{r} \quad . \quad (2.1.18)$$

Adding the two inequalities leads to

$$\Omega + \Omega' < \Omega + \Omega' \quad (2.1.19)$$

which is clearly a contradiction and therefore the assumption that two or more different external potentials lead to the same $\rho_0^{(1)}$ must be false. Thus there exists a bijective relation between V_{ext} and $\rho_0^{(1)}$ and lastly, as f_0 is a functional of V_{ext} , the Theorem is proven.

Theorem 2. Let $\rho^{(1)}(\mathbf{r})$ be a single-particle density associated with the phase space probability density f , i. e.

$$\rho^{(1)}(\mathbf{r}) = \text{Tr}[f\rho(\mathbf{r})] \quad . \quad (2.1.20)$$

Then the functional

$$\Omega_{\text{V}_{\text{ext}}}[\rho^{(1)}] = \mathcal{F}[\rho^{(1)}] + \int \rho^{(1)}(\mathbf{r})V_{\text{ext}}(\mathbf{r})d\mathbf{r} - \mu \int \rho^{(1)}(\mathbf{r})d\mathbf{r} \quad (2.1.21)$$

has its minimum if $\rho^{(1)}(\mathbf{r})$ coincides with the equilibrium single-particle density $\rho_0^{(1)}(\mathbf{r})$.

Proof. Inserting f into the grand potential functional (2.1.10) yields

$$\begin{aligned} \Omega[f] &= \text{Tr}[f(\mathcal{H} - N\mu + k_{\text{B}}T \ln f)] \\ &= \mathcal{F}[\rho^{(1)}] + \int \rho^{(1)}(\mathbf{r})V_{\text{ext}}(\mathbf{r})d\mathbf{r} - \mu \int \rho^{(1)}(\mathbf{r})d\mathbf{r} = \Omega_{\text{V}_{\text{ext}}}[\rho^{(1)}] \end{aligned} \quad (2.1.22)$$

Using the inequality (2.1.11) leads to

$$\Omega_{\text{V}_{\text{ext}}}[\rho^{(1)}] \geq \Omega_{\text{V}_{\text{ext}}}[\rho_0^{(1)}] = \Omega[f] = \Omega \quad (2.1.23)$$

which proves the Theorem. Thus the existence of a unique functional for the intrinsic free energy \mathcal{F} which solely depends on the single-particle density has been proven. This functional can be split into an ideal part which can be derived analytically and an excess part which originates from V_N and for which sensible approximations have to be made:

$$\mathcal{F}[\rho^{(1)}] = \mathcal{F}_{\text{id}}[\rho^{(1)}] + \mathcal{F}_{\text{ex}}[\rho^{(1)}] = k_{\text{B}}T \int d\mathbf{r} \rho^{(1)}(\mathbf{r})(\ln[\Lambda^3 \rho^{(1)}(\mathbf{r})] - 1) + \mathcal{F}_{\text{ex}}[\rho^{(1)}] \quad (2.1.24)$$

$\Lambda = \hbar\sqrt{2\pi/mk_{\text{B}}T}$ denotes the thermal de Broglie wavelength. For simplicity $\rho^{(1)}(\mathbf{r})$ is replaced by $\rho(\mathbf{r})$ in what follows.

2.2 The Mean Field Functional

In this section the mean field functional is derived as it was presented by Likos et al. [14] but without the restriction to spherical symmetry of the pair potential.

\mathcal{F}_{ex} can formally be expanded in a Taylor series around a reference system

with uniform density ρ_0

$$\beta\mathcal{F}_{\text{ex}}[\rho] = \beta\mathcal{F}_{\text{ex}}(\rho_0) - \sum_{n=1}^{\infty} \frac{1}{n!} \int \dots \int d^3\mathbf{r}_1 \dots d^3\mathbf{r}_n \\ * c_0^{(n)}(\mathbf{r}^n; \rho_0) (\rho(\mathbf{r}_1) - \rho_0) \dots (\rho(\mathbf{r}_n) - \rho_0) \quad (2.2.1)$$

using the fact that \mathcal{F}_{ex} is the generating functional of the n -particle direct correlation functions (DCF) $c_0^{(n)}(\mathbf{r}^n; \rho_0)$

$$c_0^{(n)}(\mathbf{r}^n; \rho_0) = - \left. \frac{\delta^n \beta\mathcal{F}_{\text{ex}}[\rho]}{\delta\rho(\mathbf{r}_1) \dots \delta\rho(\mathbf{r}_n)} \right|_{\rho=\rho_0} . \quad (2.2.2)$$

$c_0^{(2)}(\mathbf{r}_1, \mathbf{r}_2; \rho_0)$ corresponds to the Ornstein-Zernike direct correlation function [47]. The DCF related to different numbers of particles are not independent from one another as they fulfil the following relation [48–50]:

$$\int d\mathbf{r}_k c_0^{(n+1)}(\mathbf{r}_1, \dots, \mathbf{r}_{k-1}, \mathbf{r}_k, \mathbf{r}_{k+1}, \dots, \mathbf{r}_{n+1}; \rho) = \frac{\partial c_0^{(n)}(\mathbf{r}_1, \dots, \mathbf{r}_{k-1}, \mathbf{r}_{k+1}, \dots, \mathbf{r}_{n+1}; \rho)}{\partial\rho} \quad (2.2.3)$$

Within the framework of the mean field approximation (MFA), also called random phase approximation (see, for instance [46]), one assumes that

$$c_0^{(2)}(\mathbf{r}, \mathbf{r}'; \rho) = -\beta v(\mathbf{r}, \mathbf{r}') . \quad (2.2.4)$$

$v(\mathbf{r}, \mathbf{r}')$ denotes the pair interaction which is bounded, thus allowing full particle overlaps, and which fulfils the Ruelle conditions for stability [14, 51]. In the following it is assumed that the pair interaction only depends on $\mathbf{r} - \mathbf{r}'$:

$$v(\mathbf{r}, \mathbf{r}') = v(\mathbf{r} - \mathbf{r}') . \quad (2.2.5)$$

$v(\mathbf{r} - \mathbf{r}')$ has to be bounded, as $c_0^{(2)}(\mathbf{r}, \mathbf{r}'; \rho)$ has to remain finite at all $\mathbf{r} - \mathbf{r}'$ [46]. Inserting the relation (2.2.4) into Eq. (2.2.3) yields

$$\int d\mathbf{r}_3 c_0^{(3)}(\mathbf{r}_1, \mathbf{r}_2, \mathbf{r}_3; \rho) = \frac{\partial c_0^{(2)}(\mathbf{r}_1, \mathbf{r}_2; \rho)}{\partial\rho} = 0 . \quad (2.2.6)$$

The complex dependence of $c_0^{(3)}$ on its arguments is a strong indication that not only the integral but also the integrand itself vanishes [14]. This surmise

is supported by the fact that both for the Barrat-Hansen-Pastore factorization approximation for $c_0^{(3)}$ and the Denton-Ashcroft \mathbf{q} -space factorization, the DCF $c_0^{(3)}$ vanishes within the MFA framework [48, 50]. By using the same rule, Eq. (2.2.3) implies that all the higher DCF vanish, i.e.

$$c_0^{(n)}(\mathbf{r}_1, \mathbf{r}_2, \dots, \mathbf{r}_n; \rho) = 0, \quad (n \geq 3) \quad . \quad (2.2.7)$$

Thus, going back to the Taylor series of \mathcal{F}_{ex} (2.2.1) terms with $n \geq 3$ can now be omitted. Inserting $c_0^{(1)}$, which is calculated via Eq. (2.2.3), i.e.

$$\frac{\partial c_0^{(1)}(\mathbf{r}'; \rho)}{\partial \rho} = \int d\mathbf{r} c_0^{(2)}(\mathbf{r}, \mathbf{r}'; \rho) = -\beta \int d\mathbf{r} v(\mathbf{r} - \mathbf{r}') = -\beta \tilde{v}(0) \quad (2.2.8)$$

$$c_0^{(1)}(\rho) = -\beta \tilde{v}(0) \rho \quad (2.2.9)$$

and using the MFA closure relation for $c_0^{(2)}$ yields

$$\begin{aligned} \beta \mathcal{F}_{\text{ex}}[\rho] &= \beta \mathcal{F}_{\text{ex}}(\rho_0) + \beta \tilde{v}(0) \rho_0 \int d\mathbf{r} (\rho(\mathbf{r}) - \rho_0) \\ &\quad + \frac{\beta}{2} \int \int d\mathbf{r} d\mathbf{r}' v(\mathbf{r} - \mathbf{r}') (\rho(\mathbf{r}) - \rho_0) (\rho(\mathbf{r}') - \rho_0) \quad . \quad (2.2.10) \end{aligned}$$

Formally substituting $\rho_0 \rightarrow 0$ and $\rho(\mathbf{r}) \rightarrow \rho_0$ and using the fact that $\mathcal{F}_{\text{ex}}(\rho)$ and $c_0^{(1)}(\rho)$ vanish with the density leads to an energy dependence of the excess free energy of the homogeneous system

$$\begin{aligned} \beta \mathcal{F}_{\text{ex}}(\rho_0) &= \beta \mathcal{F}_{\text{ex}}(0) - c_0^{(1)}(0) \int d\mathbf{r} \rho_0 - \frac{1}{2} \int \int d\mathbf{r} d\mathbf{r}' c_0^{(2)}(\mathbf{r}, \mathbf{r}'; 0) \rho_0^2 \\ &= \frac{\beta}{2} \rho_0 \int d\mathbf{r} \rho_0 \int d\mathbf{r}' v(\mathbf{r} - \mathbf{r}') \quad (2.2.11) \\ &= \frac{N_0}{2} \beta \tilde{v}(0) \rho_0 \end{aligned}$$

where $N_0 = \int d\mathbf{r} \rho_0$ denotes the particle number of this reference system, which in general does not coincide with the particle number $N = \int d\mathbf{r} \rho(\mathbf{r})$ of the system with density $\rho(\mathbf{r})$. Inserting Eq. (2.2.11) into Eq. (2.2.10)

yields

$$\begin{aligned}
\beta\mathcal{F}_{ex}[\rho] &= \frac{N_0}{2}\beta\tilde{v}(0)\rho_0 + \beta\tilde{v}(0)\rho_0(N - N_0) \\
&+ \frac{\beta}{2} \int \int d\mathbf{r}d\mathbf{r}' v(\mathbf{r} - \mathbf{r}')\rho(\mathbf{r})\rho(\mathbf{r}') \\
&- \beta\rho_0 \int \int d\mathbf{r}d\mathbf{r}' v(\mathbf{r} - \mathbf{r}')\rho(\mathbf{r}) \\
&+ \frac{N_0}{2}\beta\tilde{v}(0)\rho_0 \quad .
\end{aligned} \tag{2.2.12}$$

Substituting $\mathbf{s} = \mathbf{r} - \mathbf{r}'$ the fourth term above becomes

$$- \beta\rho_0 \int d\mathbf{r}\rho(\mathbf{r}) \int d\mathbf{s} v(\mathbf{s}) = -\beta N\rho_0\tilde{v}(0) \quad . \tag{2.2.13}$$

This leads to the cancellation of almost all terms in Eq. (2.2.12) and the final result for \mathcal{F}_{ex} is obtained as

$$\mathcal{F}_{ex}[\rho] = \frac{1}{2} \int \int d\mathbf{r}d\mathbf{r}' v(\mathbf{r} - \mathbf{r}')\rho(\mathbf{r})\rho(\mathbf{r}') \quad . \tag{2.2.14}$$

This expression is independent of a reference system which gives rise to the fact, that it can be used to calculate the excess free energy of *any* inhomogeneous system for which the MFA closure is a reasonable choice. Of course, the neglected terms for $n \geq 3$ in (2.2.1), which are particularly important in the low temperature and/or low density domain, do not vanish exactly. However, comparisons with simulations provides evidence that this approximation is reasonable [12,15,29]. Within this approximation the grand potential functional is obtained as

$$\begin{aligned}
\beta\Omega_{\text{MFA}}[\rho] &= \int d\mathbf{r} \rho(\mathbf{r})(\ln[\Lambda^3\rho(\mathbf{r})] - 1) + \frac{\beta}{2} \int \int d\mathbf{r}d\mathbf{r}' v(\mathbf{r} - \mathbf{r}')\rho(\mathbf{r})\rho(\mathbf{r}') \\
&+ \beta \int \rho(\mathbf{r})V_{\text{ext}}(\mathbf{r})d\mathbf{r} - \beta\mu \int \rho(\mathbf{r})d\mathbf{r} \quad .
\end{aligned} \tag{2.2.15}$$

For given V_{ext} and μ the equilibrium density profiles $\rho_{\text{min}}(\mathbf{r})$ are obtained by minimizing this functional. Within this thesis only systems with $V_{\text{ext}}(\mathbf{r}) = 0$ are considered. The $\rho_{\text{min}}(\mathbf{r})$ satisfy the Euler-Lagrange equation (see, for instance [46])

$$\left. \frac{\delta(\beta\Omega_{\text{MFA}})}{\delta\rho} \right|_{\rho(\mathbf{r})=\rho_{\text{min}}(\mathbf{r})} = 0 \quad . \tag{2.2.16}$$

A homogeneous state where $\rho(\mathbf{r}) \equiv \bar{\rho}$ is a trivial solution of the Euler-Lagrange equation with the chemical potential

$$\beta\mu = \ln(\bar{\rho}\Lambda^3) + \bar{\rho} \int d\mathbf{r} \beta v(\mathbf{r}) \quad . \quad (2.2.17)$$

This equation follows from applying the Euler-Lagrange equation to such a homogeneous density profile, i.e.

$$\frac{\partial(\beta\Omega_{\text{MFA}}(\bar{\rho}))}{\partial\bar{\rho}} = 0 \quad . \quad (2.2.18)$$

Furthermore an excess chemical potential μ_{ex} is introduced, as done by Pini et al. [11], by the relation

$$\ln(\rho(\mathbf{r})\Lambda^3) - 1 - \beta\mu = \ln(\rho(\mathbf{r})/\bar{\rho}) - 1 - \beta\mu_{\text{ex}} \quad . \quad (2.2.19)$$

Eq. (2.2.17) and (2.2.19) imply that $\bar{\rho}$ and μ_{ex} satisfy the following relation:

$$\beta\mu_{\text{ex}} = \bar{\rho} \int d\mathbf{r} \beta v(\mathbf{r}) \quad . \quad (2.2.20)$$

Using Eq. (2.2.19) the grand potential functional can be written as

$$\beta\Omega_{\text{MFA}}[\rho] = \int d\mathbf{r} \rho(\mathbf{r})(\ln[\rho(\mathbf{r})/\bar{\rho}] - 1 - \beta\mu_{\text{ex}}) + \frac{\beta}{2} \int \int d\mathbf{r}d\mathbf{r}' v(\mathbf{r} - \mathbf{r}')\rho(\mathbf{r})\rho(\mathbf{r}') \quad . \quad (2.2.21)$$

For a given pair potential $v(\mathbf{r} - \mathbf{r}')$ the only external parameters for the functional above are $\bar{\rho}$ and the temperature T .

2.3 The System

In this thesis an anisometric ultrasoft potential is considered, the generalization of the generalized exponential functions (GEM-n)

$$v(r) = \varepsilon \exp[-(r/\sigma)^n] \quad (2.3.1)$$

with an energy scale ε and a length scale σ . It can be shown [14] that GEM-n potentials with $n > 2$ belong to the so called \mathcal{Q}^\pm class [29], which means that their Fourier transform has a negative minimum at $|\mathbf{q}| \neq 0$. This feature is

a necessary condition for the formation of clusters of overlapping particles, while the interactions with a nonnegative Fourier transform (belonging to the \mathcal{Q}^+ class) do not lead to clustering [13, 16, 52–55]. Especially systems where particles interact via the GEM-4 potentials have been studied thoroughly using computer simulations and DFT calculations which lead to the prediction of body-centered cubic (bcc) and face-centered cubic (fcc) cluster crystals [14, 15]. The DFT results for the free energies were found to be in excellent agreement with Monte Carlo simulations [14].

In the present thesis a generalized version of this type of interaction is considered which introduces anisotropy. This modified GEM- n potential is given by

$$v(\mathbf{r}; \mathbf{u}, \mathbf{u}') = \varepsilon(\mathbf{r}; \mathbf{u}, \mathbf{u}') \exp \left[- \left(\frac{r}{\sigma(\mathbf{r}; \mathbf{u}, \mathbf{u}')} \right)^n \right] \quad (2.3.2)$$

where \mathbf{u} and \mathbf{u}' are the orientational unit-vectors of the now anisometric particles. Within this thesis only the case $n = 4$ was treated. Fig. 2.1 shows a sketch of two interacting particles, indicated by the vectors \mathbf{r} , \mathbf{u} and \mathbf{u}' .

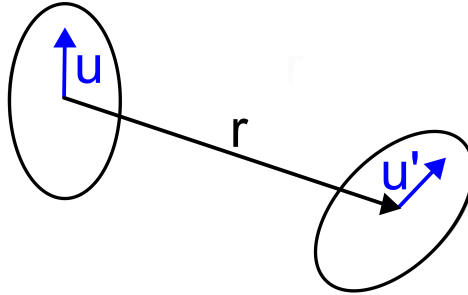


Figure 2.1: Schematic illustration of two interacting anisometric particles. \mathbf{u} and \mathbf{u}' denote the orientational unit vectors of the respective particles and \mathbf{r} is the center-to-center vector [56]

Different choices for the dependence of σ and ε on \mathbf{r} , \mathbf{u} and \mathbf{u}' are available in literature. In this thesis the expression for $\sigma(\mathbf{r}; \mathbf{u}, \mathbf{u}')$ is given by

$$\sigma(\mathbf{r}; \mathbf{u}, \mathbf{u}') = \sigma_0 \left(1 - \frac{\chi}{r^2} \frac{(\mathbf{r} \cdot \mathbf{u})^2 + (\mathbf{r} \cdot \mathbf{u}')^2 - 2\chi(\mathbf{r} \cdot \mathbf{u})(\mathbf{r} \cdot \mathbf{u}')(\mathbf{u} \cdot \mathbf{u}')}{1 - \chi^2(\mathbf{u} \cdot \mathbf{u}')^2} \right)^{-1/2} \quad (2.3.3)$$

as proposed by Ghoufi et al. [57] introducing the anisotropy parameter $\chi = (\lambda^2 - 1)/(\lambda^2 + 1)$ and the aspect ratio $\lambda = \sigma_{\parallel}/\sigma_{\perp}$ between the major and the minor axis of the interacting particles. In contrast to Ghoufi et al., the energy scale parameter is assumed to be constant:

$$\varepsilon(\mathbf{r}; \mathbf{u}, \mathbf{u}') = \varepsilon \quad . \quad (2.3.4)$$

Within this work the orientational unit-vectors of the particles populating a lattice are assumed to be parallel. Their direction is arbitrary in space but it is kept fixed throughout the calculations.

Setting $\mathbf{u} = \mathbf{u}' = \mathbf{n}$ with $|\mathbf{n}| = 1$ and $\varepsilon(\mathbf{r}; \mathbf{u}, \mathbf{u}') = \varepsilon$ leads to the following expressions

$$v(\mathbf{r}) = \varepsilon \exp \left[- \left(\frac{r}{\sigma(\mathbf{r})} \right)^4 \right] \quad , \quad (2.3.5)$$

$$\sigma(\mathbf{r}) = \frac{\sigma_0}{\sqrt{1 + (\lambda^{-2} - 1) \left(\frac{\mathbf{r} \cdot \mathbf{n}}{r} \right)^2}} \quad . \quad (2.3.6)$$

A schematic illustration of two particles interacting via this potential is shown in Fig. 2.2. Setting $\lambda = 1$ corresponds to the spherically symmetric case of Eq. (2.3.1). As

$$\left(\frac{\mathbf{r} \cdot \mathbf{n}}{r|\mathbf{n}|} \right)^2 = \left(\frac{\mathbf{r} \cdot \mathbf{n}}{r} \right)^2 = \cos^2(\vartheta) \quad (2.3.7)$$

the pair potential can be written as $v(r, \vartheta)$ which depends on the distance r and on the angle ϑ between \mathbf{r} and \mathbf{n} as shown in Fig. 2.3 and 2.4. Similarly, the Fourier transform $\tilde{v}(\mathbf{q})$ of the pair potential can be written as $\tilde{v}(q, \phi)$ where $q = |\mathbf{q}|$ and ϕ is the angle enclosed by \mathbf{q} and the preferred axis in q -space (Fig. 2.5 and 2.6). It is notable that in the spherically symmetric case the position of the minima of $\tilde{v}(\mathbf{q})$ only depends on $|\mathbf{q}|$, whereas for $\lambda > 1.0$ the position of the minima also shows angular dependence in q -space. Their respective values however turn out to be independent of q and ϕ .

Note that the the anisometry in the pair potential given by Eq. (2.3.5) and (2.3.6) has a huge impact on whether two systems are equivalent or not. If no direction in space is preferred the physics of a system do not depend on its orientation. Two systems are equivalent if they can be transformed into

each other by *any* rotation. However, if the rotational symmetry of the pair potential is broken by introducing a preferred axis only systems that are connected by a rotation around this axis are equivalent.

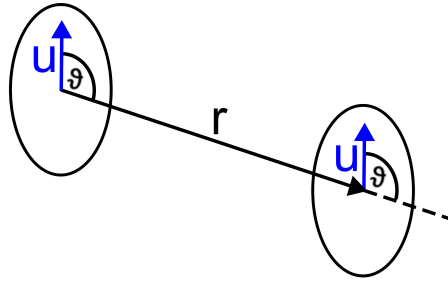


Figure 2.2: Schematic illustration of two parallel particles interacting via the potential given in Eq. (2.3.5) and (2.3.6). \mathbf{n} denotes the orientational unit vector of both particles, \mathbf{r} is the center-to-center vector and ϑ is the angle enclosed by \mathbf{n} and \mathbf{r} .

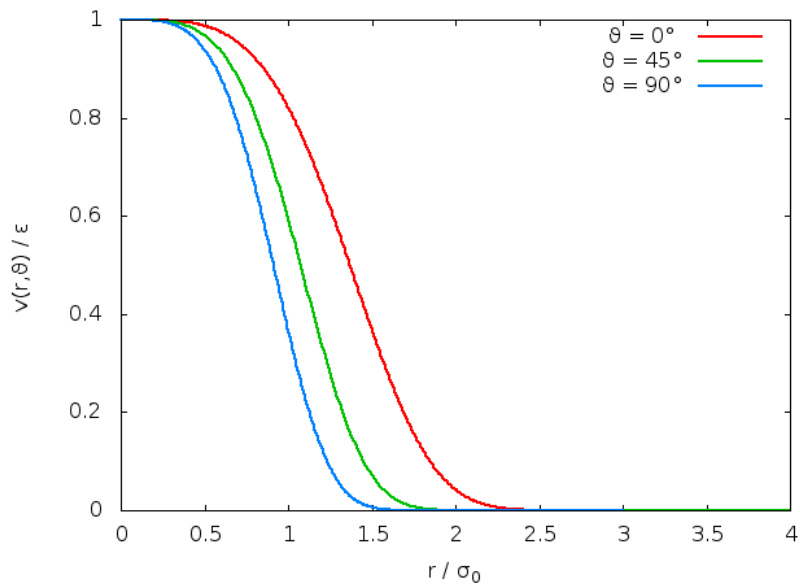


Figure 2.3: Dependence of the pair potential $v(r, \vartheta)$ in units of ϵ on r for $\vartheta = 0^\circ$, $\vartheta = 45^\circ$ and $\vartheta = 90^\circ$ for $\lambda = 1.5$.

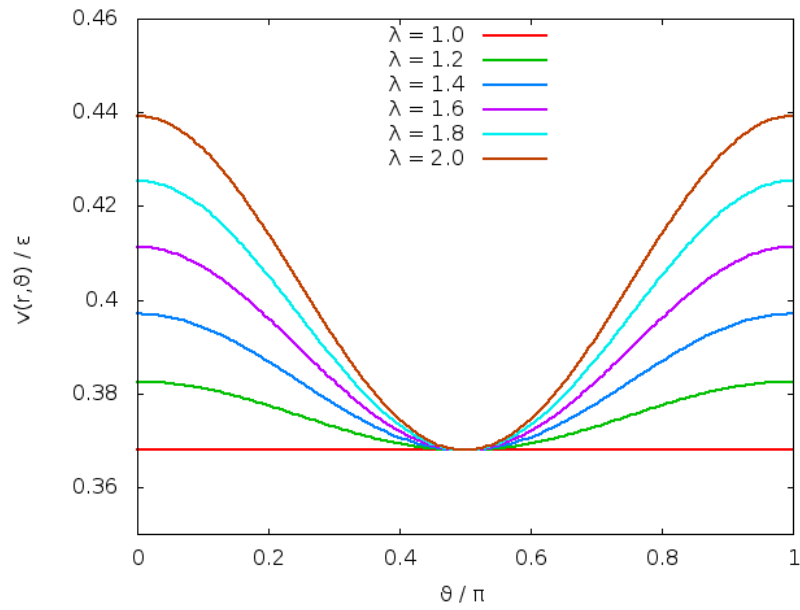


Figure 2.4: Dependence of the pair potential $v(r, \vartheta)$ in units of ε on ϑ for different values of λ as labeled with a fixed $r = \sigma_0$.

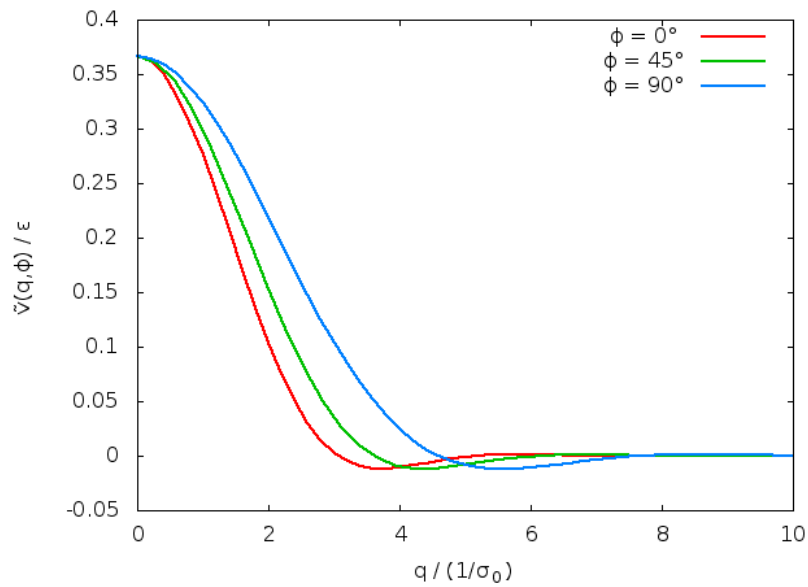


Figure 2.5: Dependence of the Fourier transform of the pair potential $\tilde{v}(q, \phi)$ in units of ε on q for $\phi = 0^\circ$, $\phi = 45^\circ$ and $\phi = 90^\circ$ for $\lambda = 1.5$.

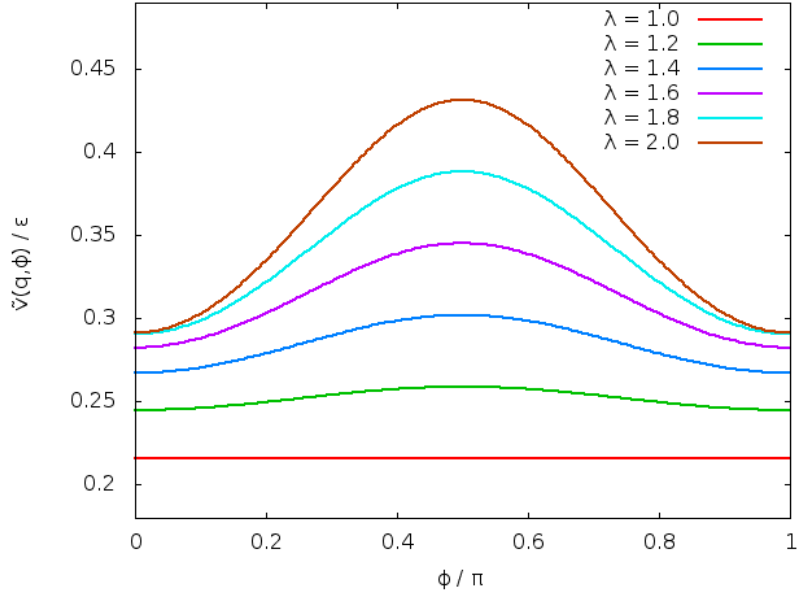


Figure 2.6: Dependence of the Fourier transform of the pair potential $\tilde{v}(q, \phi)$ in units of ϵ on ϕ for different values of λ as labeled with a fixed $q = 1/\sigma_0$.

2.4 Shape and Orientation Analysis of the Single-particle Density Profile

In an effort to analyse and identify single-particle density profiles, two quantities will be introduced in the following which characterize their shape:

(i) the radius of gyration R_g and (ii) the radius of gyration Tensor \mathcal{S} . R_g is a fundamental quantity for characterizing the size of complex particles [58]. Usually it is defined for a macromolecule consisting of N entities, i. e. (see, for example [59])

$$R_g^2 = \frac{1}{N} \sum_{i=1}^N (\mathbf{r}_i - \mathbf{R}_{\text{cm}})^2 \quad (2.4.1)$$

where the \mathbf{r}_i are the position vectors of the entities and \mathbf{R}_{cm} is the position vector of the center of mass. The latter is given by

$$\mathbf{R}_{\text{cm}} = \frac{1}{N} \sum_{i=1}^N \mathbf{r}_i \quad . \quad (2.4.2)$$

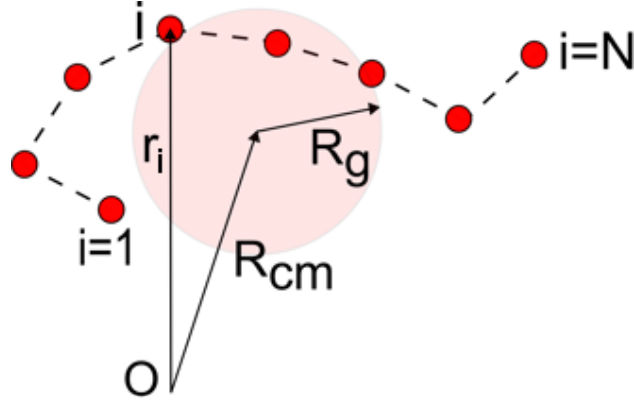


Figure 2.7: Schematic illustration of the radius of gyration R_g for a chain consisting of N entities. O is the origin, \mathbf{R}_{cm} is the center-of-mass vector and \mathbf{r}_i is the position vector of the i -th entity (redrawn from [59]).

Fig. 2.7 illustrates the radius of gyration of a polymer. In a similar manner, one can define R_g and \mathbf{R}_{cm} for a continuous single-particle density as

$$R_g^2 = \frac{1}{N} \int d\mathbf{r} \rho(\mathbf{r})(\mathbf{r} - \mathbf{R}_{\text{cm}})^2 \quad (2.4.3)$$

with

$$\mathbf{R}_{\text{cm}} = \frac{1}{N} \int d\mathbf{r} \rho(\mathbf{r})\mathbf{r} \quad (2.4.4)$$

where \mathbf{r} and $(\mathbf{r} - \mathbf{R}_{\text{cm}})^2$ are weighted by $\rho(\mathbf{r})$.

Characterizing the density profile solely via the radius of gyration is useful for spherically symmetric systems, for example in the spherically symmetric GEM-4 model (see, for instance [11] or section 3.4). However, the characterization of the density profile via the radius is in general not sufficient. Therefore one needs to make use of the radius of gyration tensor (RGT) denoted by \mathcal{S} [60]. For a macromolecule consisting of N entities the components \mathcal{S}_{ij} are given by (see, for instance [59])

$$\mathcal{S}_{ij} = \frac{1}{N} \sum_{n=1}^N (r_{n,i} - R_{\text{cm},i})(r_{n,j} - R_{\text{cm},j}) \quad (2.4.5)$$

or in the continuous case

$$\mathcal{S}_{ij} = \frac{1}{N} \int d\mathbf{r} \rho(\mathbf{r})(r_i - R_{\text{cm},i})(r_j - R_{\text{cm},j}) \quad (2.4.6)$$

The $r_{n,i}$ are the components of the position vector $\mathbf{r}_n = (r_{n,1}, r_{n,2}, r_{n,3})$. Thus, the RGT is given by

$$\begin{aligned} \mathcal{S} &= \begin{bmatrix} \mathcal{S}_{11} & \mathcal{S}_{12} & \mathcal{S}_{13} \\ \mathcal{S}_{21} & \mathcal{S}_{22} & \mathcal{S}_{23} \\ \mathcal{S}_{31} & \mathcal{S}_{32} & \mathcal{S}_{33} \end{bmatrix} \\ &= \begin{bmatrix} \langle (r_1 - R_{\text{cm},1})^2 \rangle & \langle (r_1 - R_{\text{cm},1})(r_2 - R_{\text{cm},2}) \rangle & \langle (r_1 - R_{\text{cm},1})(r_3 - R_{\text{cm},3}) \rangle \\ \langle (r_2 - R_{\text{cm},2})(r_1 - R_{\text{cm},1}) \rangle & \langle (r_2 - R_{\text{cm},2})^2 \rangle & \langle (r_2 - R_{\text{cm},2})(r_3 - R_{\text{cm},3}) \rangle \\ \langle (r_3 - R_{\text{cm},3})(r_1 - R_{\text{cm},1}) \rangle & \langle (r_3 - R_{\text{cm},3})(r_2 - R_{\text{cm},2}) \rangle & \langle (r_3 - R_{\text{cm},3})^2 \rangle \end{bmatrix} \end{aligned} \quad (2.4.7)$$

where $\langle \dots \rangle$ is shorthand for $1/N \int d\mathbf{r} \rho(\mathbf{r})(\dots)$. By definition, \mathcal{S}_{ij} is symmetric and real. One can easily verify, that $R_{\text{g}}^2 = \mathcal{S}_{11} + \mathcal{S}_{22} + \mathcal{S}_{33} = \text{Tr}(\mathcal{S})$ which is independent of the chosen basis (see, for instance [61]).

Diagonalization of the RGT leads to

$$\mathcal{S}_{\text{diag}} = \begin{bmatrix} E_1 & 0 & 0 \\ 0 & E_2 & 0 \\ 0 & 0 & E_3 \end{bmatrix} \quad (2.4.8)$$

where the E_i are the three eigenvalues to the corresponding eigenvectors \mathbf{e}_i which are mutually orthogonal. Without loss of generality it is assumed that $E_1 \geq E_2 \geq E_3$. Characterizing the density profile $\rho(\mathbf{r})$ by the eigenvalues of the RGT corresponds to approximating the shape of $\rho(\mathbf{r})$ by an ellipsoid located at \mathbf{R}_{cm} : the eigenvectors are the principal axes and the square roots of the eigenvalues $\sqrt{E_i}$ correspond to the lengths of the semi-axes of the ellipsoid [59]. Two further quantities which characterize the shape of the density profile are the asphericity parameter δ , given by the definition of Rudnick and Gaspari [62], and the acylindricity parameter ζ , given by the definition of Georgiou [59]:

$$\delta = 1 - 3 \frac{E_1 E_2 + E_1 E_3 + E_2 E_3}{(E_1 + E_2 + E_3)^2} \quad , \quad (2.4.9)$$

$$\zeta = E_2 - E_3 \quad , \quad \zeta \geq 0 \quad . \quad (2.4.10)$$

δ ranges from 0 (for spherical symmetry) to 1 (for a rod-like shape).

Chapter 3

Minimization Method

In the preceding chapter the mean field functional (2.2.21), which forms the basis for all the calculations within this thesis was derived and the modified GEM-4 pair potential was presented.

In this chapter the details of the numerical minimization of this functional, which relies heavily on preceding work of Pini et al. [11], are explained. The first two sections of this chapter focus on the assumptions that are made for the single-particle density profile and on how a numerically treatable expression for the functional can be derived. The third chapter gives an overview on how the minimization is actually performed. In the fourth chapter tests of the reliability of this minimization are presented by applying the algorithm to the GEM-4 model for which extensive results are already available.

3.1 Basic Assumptions for the Density Profile

As ordered structures are to be investigated, the first basic assumption on the density profile is that $\rho(\mathbf{r})$ is a periodic function of \mathbf{r} :

$$\rho(\mathbf{r} + \mathbf{a}_i) = \rho(\mathbf{r}) \quad , \quad i = 1, 2, 3 \quad . \quad (3.1.1)$$

The vectors \mathbf{a}_i generate a Bravais lattice where any point of the lattice, \mathbf{R}_n , can be represented by

$$\mathbf{R}_n = \sum_{i=1}^3 n_i \mathbf{a}_i \quad , \quad n_i \in \mathbb{Z} \quad . \quad (3.1.2)$$

The \mathbf{a}_i form the unit cell, thus any point \mathbf{x} within the unit cell can be written as

$$\mathbf{x} = \sum_{i=1}^3 x_i \mathbf{a}_i \quad , \quad -\frac{1}{2} \leq x_i < \frac{1}{2} \quad . \quad (3.1.3)$$

Therefore, any point of space can be written as $\mathbf{r} = \mathbf{x} + \mathbf{R}_n$. If \mathbf{A} denotes the matrix obtained by arranging the \mathbf{a}_i into columns

$$\mathbf{A} = (\mathbf{a}_1, \mathbf{a}_2, \mathbf{a}_3) \quad , \quad (3.1.4)$$

then the volume of the unit cell, v , is calculated via $v = |\det(\mathbf{A})|$. In the following, the generating vectors of the corresponding reciprocal lattice are denoted by \mathbf{b}_i . They fulfil the relations $\mathbf{a}_i \cdot \mathbf{b}_j = 2\pi\delta_{ij}$ where δ_{ij} is the Kronecker-Delta [63].

By assuming periodicity of the density profile the numerical effort to calculate $\rho(\mathbf{r})$ at any position $\mathbf{r} \in \mathbb{R}^3$ is drastically reduced. It is now sufficient to calculate the density profile within a single unit cell $\rho(\mathbf{x})$.

The second assumption being imposed on the density profile is that it is discretized at a set of N^3 points of the unit cell:

$$\rho(\mathbf{x}) \mapsto \rho(\mathbf{x}_n) = \rho_n \quad (3.1.5)$$

where

$$\mathbf{x}_n = \sum_{i=1}^3 \frac{n_i}{N} \mathbf{a}_i \quad , \quad -\frac{N}{2} \leq n_i < \frac{N}{2} \quad , \quad n_i \in \mathbb{Z} \quad . \quad (3.1.6)$$

Hence, the *functional* $\Omega[\rho]$ reduces to a *function* $\Omega(\rho_n; \mathbf{b}_i)$. This function now depends on N^3 variables for the density profile and (in general) on nine variables that define the Bravais lattice:

$$\Omega[\rho] \mapsto \Omega(\rho_n; \mathbf{b}_i) \quad . \quad (3.1.7)$$

Possible rotational symmetries of the system can further reduce the number of variables defining the lattice. Note that one could have equivalently chosen the \mathbf{a}_i as variables, as there is a one-to-one correspondence between the direct and the reciprocal lattice. The \mathbf{b}_i are preferred to the \mathbf{a}_i purely for computational reasons.

3.2 Deriving a Numerically Treatable Expression for the Functional

As $\Omega(\rho_{\mathbf{n}}; \mathbf{b}_i)$ is an extensive quantity it is hence forward divided by the volume V of the system:

$$\frac{\beta\Omega(\rho_{\mathbf{n}}; \mathbf{b}_i)}{V} = \frac{\beta\mathcal{F}_{\text{id}}(\rho_{\mathbf{n}})}{V} + \frac{\beta\mathcal{F}_{\text{ex}}(\rho_{\mathbf{n}}; \mathbf{b}_i)}{V} - \frac{\beta\mu}{V} \int d\mathbf{r} \rho(\mathbf{r}) \quad (3.2.1)$$

As the integrand of the first and the third term on the right-hand side of the above relation is periodic one can rewrite them as

$$\frac{\beta\mathcal{F}_{\text{id}}(\rho_{\mathbf{n}})}{V} - \frac{\beta\mu N}{V} = \frac{1}{N^3} \sum_{\mathbf{n}} \rho_{\mathbf{n}} [\ln(\rho_{\mathbf{n}}/\bar{\rho}) - 1 - \beta\mu_{\text{ex}}] \quad (3.2.2)$$

where the summation is only performed over all grid points within the unit cell.

Due to the lack of periodicity of $v(\mathbf{r})$, this approach cannot be applied to the second term. Instead, the excess part of the functional as given by Eq. (2.2.14) can be rewritten by expanding the density profile in a Fourier series

$$\rho_{\mathbf{n}} = \rho(\mathbf{x}_{\mathbf{n}}) = \frac{1}{v} \sum_{\mathbf{m}} e^{-i\mathbf{q}_{\mathbf{m}} \cdot \mathbf{x}_{\mathbf{n}}} \check{\rho}_{\mathbf{m}} \quad (3.2.3)$$

with

$$\check{\rho}_{\mathbf{m}} = \frac{v}{N^3} \sum_{\mathbf{n}} e^{i\mathbf{q}_{\mathbf{m}} \cdot \mathbf{x}_{\mathbf{n}}} \rho_{\mathbf{n}} := \frac{v}{N^3} \hat{\rho}_{\mathbf{m}} \quad (3.2.4)$$

where $\mathbf{q}_{\mathbf{m}} = \sum_{i=1}^3 m_i \mathbf{b}_i$ is a vector of the reciprocal lattice with $m_i \in \mathbb{Z}, i = 1, 2, 3$. Using the definition of $\mathbf{x}_{\mathbf{n}}$ (3.1.6) one arrives at

$$\rho_{\mathbf{n}} = \frac{1}{N^3} \sum_{\mathbf{m}} e^{-2\pi i \mathbf{m} \cdot \mathbf{n}/N} \hat{\rho}_{\mathbf{m}} \quad (3.2.5)$$

and

$$\hat{\rho}_{\mathbf{m}} = \sum_{\mathbf{n}} e^{2\pi i \mathbf{m} \cdot \mathbf{n} / N} \rho_{\mathbf{n}} \quad . \quad (3.2.6)$$

The Fourier transform of the pair potential is given by

$$\tilde{v}(\mathbf{q}_{\mathbf{m}}) = \int d\mathbf{r} e^{-i\mathbf{q}_{\mathbf{m}} \cdot \mathbf{r}} v(\mathbf{r}) \quad (3.2.7)$$

with its inverse Fourier transform being calculated via

$$v(\mathbf{r}) = \frac{1}{(2\pi)^3} \int d\mathbf{q} e^{i\mathbf{q} \cdot \mathbf{r}} \tilde{v}(\mathbf{q}) \quad . \quad (3.2.8)$$

Using Eq. (3.2.8), (3.2.6) and (3.2.2) leads to the final expression for the discretized grand potential functional

$$\frac{\beta \Omega_D(\rho_{\mathbf{n}}; \mathbf{b}_i)}{V} = \frac{1}{N^3} \sum_{\mathbf{n}} \rho_{\mathbf{n}} [\ln(\rho_{\mathbf{n}} / \bar{\rho}) - 1 - \beta \mu_{ex}] + \frac{\beta}{2N^6} \sum_{\mathbf{m}} \hat{\rho}_{\mathbf{m}} \hat{\rho}_{-\mathbf{m}} \tilde{v}(\mathbf{q}_{\mathbf{m}}) \quad (3.2.9)$$

which now consists of a sum over the unit cell of the direct lattice and a sum over the reciprocal lattice. Note that the lattice enters only via the reciprocal lattice vectors $\mathbf{q}_{\mathbf{m}}$ at which the Fourier transform of the pair potential $\tilde{v}(\mathbf{q}_{\mathbf{m}})$ is determined. This is the reason why the optimization with respect to \mathbf{b}_i is preferred to the optimization with respect to \mathbf{a}_i .

3.3 Minimization Algorithm

The algorithm used to perform the numerical minimization of the grand potential functional (3.2.9) is in principle the same as the one introduced by Pini et al. [11], namely a preconditioned conjugate-gradient method. For a detailed presentation of this type of algorithm see, for instance, [64]. In contrast to Pini et al. the minimization of the lattice is not only performed for an orthogonal unit cell (defined by three parameters) but for an arbitrary, possibly non-orthogonal unit cell, i.e. with respect to all nine components of the \mathbf{b}_i . In principle eight parameters are sufficient to specify such a cell because systems which act via an anisometric pair potential as the one described in Eq. (2.3.5) and (2.3.6) are invariant under rotations around the

preferred axis \mathbf{n} . However, performing an optimization with respect to eight parameters would make the implementation of the code more complicated.

In the following only the general outline of the algorithm will be described, the details are illustrated in Appendix A. The preconditioned conjugate-gradient algorithm is an advancement of the basic steepest descent method [64]. The basic principle of the steepest descent algorithm is that the free variables are constantly updated by moving in parameter space in the opposite direction of the gradient ("downhill") until convergence is reached. The preconditioned conjugate-gradient algorithm considers two refinements which increase the numerical efficiency: firstly, the Jacobi preconditioner is used in order to deform the energy surface, rendering thus plain regions less elongated [11]; secondly, the "downhill" direction is calculated by a linear combination of the gradient and the previous "downhill" direction [65].

The preconditioned conjugate-gradient algorithm performs an *unconstrained* optimization of the functional with respect to the variables. This means that no assumptions are imposed on the single-particle density profiles as long as those functions are positive. This allows to perform the minimization within the grand canonical ensemble, where the external parameters are T and μ . In principle one would obtain the same results by minimizing the free energy functional $\beta F[\rho] = \beta \Omega[\rho] + \beta \mu \int d\mathbf{r} \rho(\mathbf{r})$ with the external parameters T and N . However using a free energy functional is not suitable for an unconstrained minimization as done within this thesis as this would impose the constraint that N is kept fixed throughout the optimization.

The drawback of performing the optimization within the grand canonical ensemble is that there is no *a priori* knowledge of the resulting mean value $\langle \rho \rangle$ of the density profile, $\langle \rho \rangle$ being given by the number of particles within a cell over the volume of a cell, i. e.: $\langle \rho \rangle = n_c/v_c = 1/N^3 \sum_{\mathbf{n}} \rho_{\mathbf{n}}$. If one wants to calculate the free energy for a certain value of $\langle \rho \rangle$, the following consideration comes into play: in Sec. 2.2, $\bar{\rho}$ was introduced which corresponds to the average density of a homogeneous state minimizing the functional, given a certain excess chemical potential μ_{ex} . $\bar{\rho}$ and μ_{ex} are related via Eq. (2.2.20).

Hence, one can express the excess chemical potential in the grand potential functional in terms of $\bar{\rho}$ which provides a good estimate for the resulting mean value of the density profile $\langle\rho\rangle$. If the resulting $\rho(\mathbf{r})$ is homogeneous, i.e., constant, its mean value $\langle\rho\rangle$ coincides with $\bar{\rho}$. For non-homogeneous density profiles $\langle\rho\rangle$ is in general larger than $\bar{\rho}$, but not far off (see Fig. 3.1).

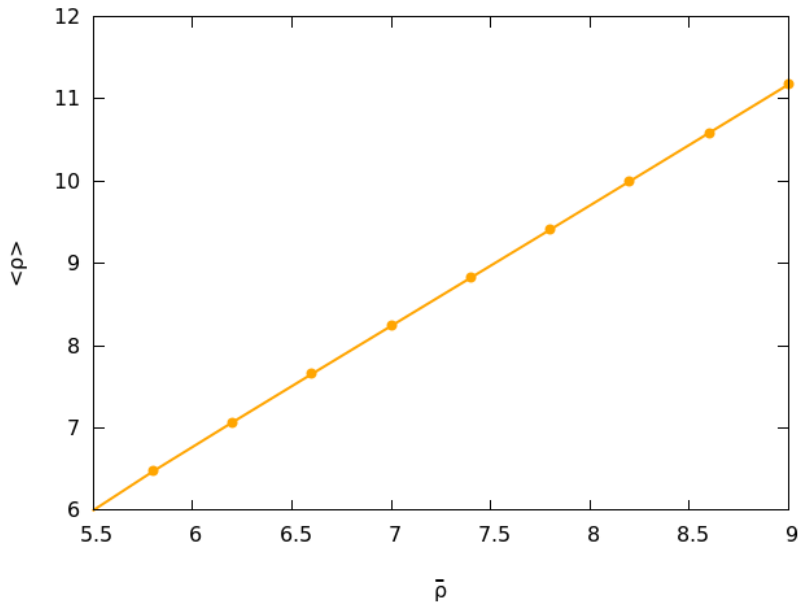


Figure 3.1: Dependence of the mean value of the density profile $\langle\rho\rangle$ on $\bar{\rho}$ for the bcc-phase of the spherical GEM-4 model with fixed temperature $k_{\text{B}}T/\varepsilon = 1.0$.

The density profile within the unit cell was usually sampled at $80 \times 80 \times 80$ points (i.e., $N = 80$) and Fourier transforms were calculated via the FFTW-package [66]. The optimization algorithm involves at several occasions sums over the reciprocal lattice. In principle, this would require a summation over an infinite number of contributions. Fortunately, it is sufficient to perform the summation over a limited number of neighbouring reciprocal lattice sites. For a detailed explanation see Appendix B.

As all the numerical calculations are very time-consuming use of shared memory parallelization via OpenMP was imperative. For a detailed explanation on shared memory parallelization in general and on OpenMP see [67]. The calculations were carried out at the Vienna Scientific Cluster [68].

3.4 The Spherical GEM-4 Model

Before considering the modified GEM-4 Model as discussed in Sec. 2.3, the reliability of the minimization algorithm is tested by applying it to the spherical GEM-4 model for which extensive results are already available [11, 14, 15]. The GEM-4 interaction is given by

$$v(r) = \varepsilon \exp[-(r/\sigma)^4] \quad . \quad (3.4.1)$$

It is an element of the \mathcal{Q}^\pm class of potentials [29]. In what follows it is useful to introduce reduced quantities $T^* = k_B T / \varepsilon$ and $\rho^* = \langle \rho \rangle \sigma^3$.

In the following, consistency with the results of Pini et al. [11] is demonstrated: these authors themselves showed that their results were in excellent agreement of those presented in Ref. [14] and [15] where the density profile was assumed to consist of a superposition of Gaussian exponential functions located at every lattice site of the Bravais lattice. In Ref. [14] the authors also performed Monte Carlo simulations which confirmed the validity of their DFT calculations. In Fig. 3.2 the values for the free energy densities are compared for several densities and two temperatures $T^* = 1.0$ and $T^* = 1.1$ with the results of Pini et al. [11]. On the scale of the figure their values are undistinguishable. Pini et al. [11] showed that the energies calculated via the Gaussian parametrization in Ref. [14] and Ref. [15] are very close to the energies of the unconstrained minimization. This can be understood by considering the resulting density profiles shown in Fig. 3.3 for selected state points. The deviations of the density profile obtained by the unconstrained minimization from a Gaussian parametrization are small. This explains why the Gaussian parametrization already yields very accurate results. Furthermore it can be observed that the density profiles are spherically symmetric, as they only depend on r . Fig. 3.4 shows the unit cells of the bcc-lattice and the fcc-lattice and isosurfaces for the single-particle density.

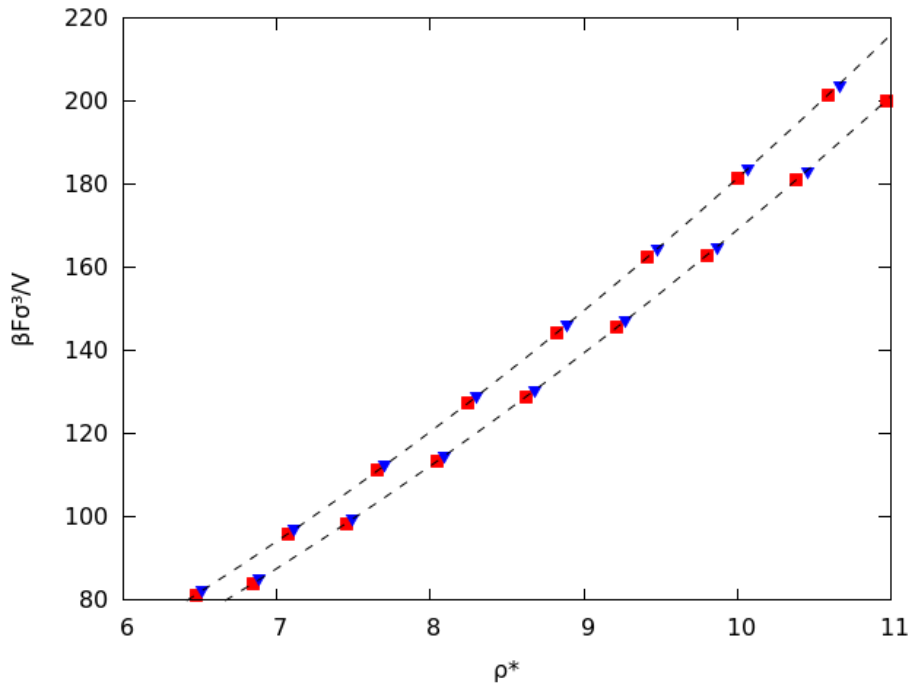


Figure 3.2: Reduced free energy density $\beta F \sigma^3 / V$ as a function of the reduced density ρ^* at two temperatures, $T^* = 1.0$ (upper curve) and $T^* = 1.1$ (lower curve). The blue triangles correspond to the fcc-phase and the red squares to the bcc-phase. A thermodynamically irrelevant shift of $\rho^*/(2T^*)$ in the energy has been subtracted from the results in order to match the definition in Ref. [14]. The dashed lines correspond to the results of Ref. [11], the red squares to the bcc-phase and the blue triangles to the fcc-phase.

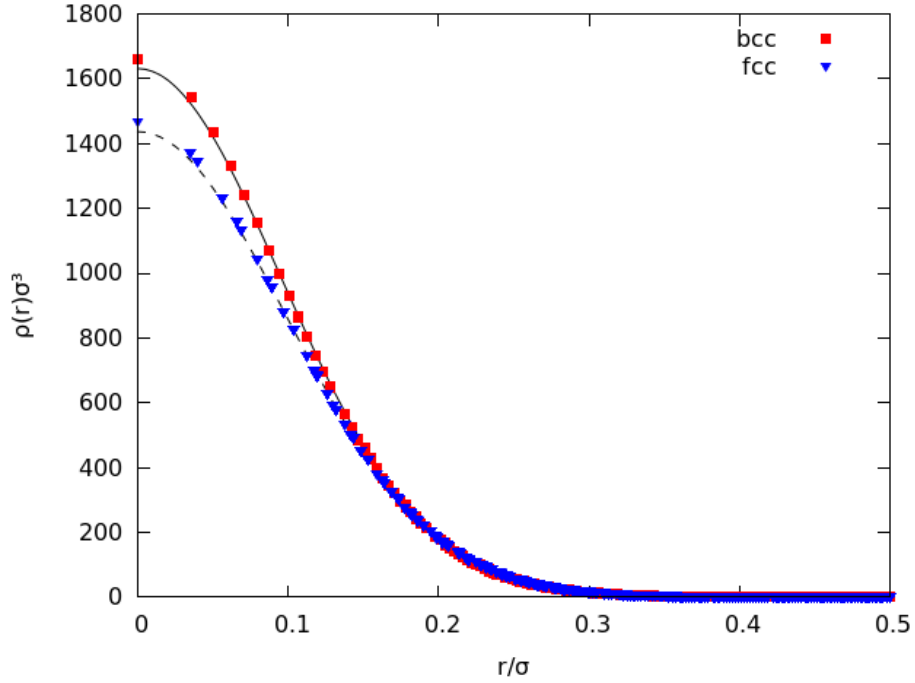


Figure 3.3: $\rho(r)$ as a function of r for $T^* = 1.0$ and $\bar{\rho} = 9.0$. The symbols correspond to the bcc-phase (red squares) and the fcc-phase (blue triangles), respectively. The solid lines are fits of a Gaussian function $f(r) = A \exp[-(r/B)^2]$ to the data. bcc-phase: $A = 1631.70$, $B = 0.134419$; fcc-phase: $A = 1436.97$, $B = 0.139143$.

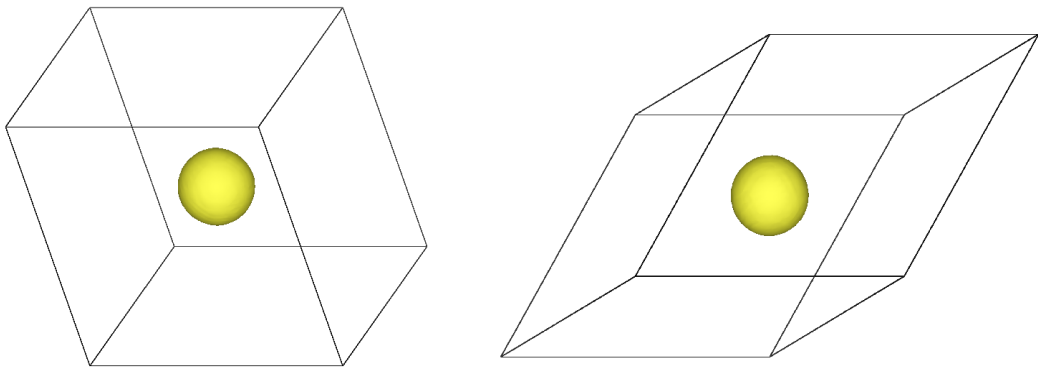


Figure 3.4: Unit cell of the lattice with isosurfaces of the single-particle density of (left) bcc-phase with isosurface for $\rho(\mathbf{r})\sigma_0^3 \equiv 150.957$ and (right) fcc-phase with isosurface for $\rho(\mathbf{r})\sigma_0^3 \equiv 161.075$.

Chapter 4

Results

In this chapter the resulting microphases of systems which interact via an anisometric, ultrasoft potential are presented. For the analytic form of the potential (and the related discussion) see Sec. 2.3. This chapter is organized as follows: in Sec. 4.1, the effects of introducing anisometry to the bcc-phase of the spherical GEM-4 model are investigated. In Sec. 4.2 the results of a general search for microphases in a system interacting via a modified GEM-4 potential with fixed anisometry-parameter $\lambda = 1.5$ are presented.

4.1 Introducing Anisometry into the GEM-4 model

In order to study the effects of a broken spherical symmetry of the potential on the density profile, the bcc-phase of the GEM-4 model is chosen as a starting point and the anisometry parameter λ is gradually increased from 1.0 to 1.5 with a fixed stepsize of 0.05; temperature and density are kept fixed: $T^* = 1.0$ and $\bar{\rho} = 7.0$. At every step, the density profile and the lattice vectors are updated via the unconstrained minimization. Note that the following results depend on the chosen representation of the bcc unit-cell of the spherical GEM-4 model. While the specific representation of the lattice is irrelevant for spherically symmetric interactions, it has a substantial impact on the resulting lattice once this symmetry is broken. In the following,

the basis vectors for the bcc-lattice are chosen to be

$$\mathbf{a}_1 = \begin{pmatrix} 0.7964 \\ 0.7964 \\ -0.7964 \end{pmatrix}, \quad \mathbf{a}_2 = \begin{pmatrix} -0.7964 \\ 0.7964 \\ 0.7964 \end{pmatrix}, \quad \mathbf{a}_3 = \begin{pmatrix} 0.7964 \\ -0.7964 \\ 0.7964 \end{pmatrix}, \quad (4.1.1)$$

in units of σ_0 . The preferred orientation of the the potential is chosen to be parallel to the x -axis, i.e.

$$\mathbf{n} = \begin{pmatrix} 1 \\ 0 \\ 0 \end{pmatrix}. \quad (4.1.2)$$

Quantitatively, the effects of the anisotropy of the particle interaction on the density profile within the unit cell can be illustrated by the tools discussed in Sec. 2.4. The change of the asphericity δ of the density profile with respect to λ is plotted in Fig. 4.1. At $\lambda = 1.0$, the asphericity vanishes, hence, the density profile is spherically symmetric. For increasing λ , the parameter δ is monotonously increasing. Two other quantities which reflect the anisotropy of the density profile are the ratios of the square roots of the eigenvalues of the RGT: $\sqrt{E_1/E_2}$ and $\sqrt{E_1/E_3}$ (see Fig. 4.2). These values quantify the semi-axes of an ellipsoid that approximates the density profile. From these data it can be concluded that the asphericity of the potential is directly reflected by the ellipsoidal symmetry of the density profile, as $\sqrt{E_1/E_2} \simeq \lambda$ and $\sqrt{E_1/E_3} \simeq \lambda$. Hence, the aspect ratio of the density profile is equal to the one of the interaction potential.

The orientation of the density profile, expressed via the principal axes \mathbf{e}_i of the ellipsoid, with respect to the preferred axis \mathbf{n} is shown in Fig. 4.3. In the spherically symmetric case, i.e. $\lambda = 1.0$, no direction is preferred and therefore the orientation of the principal axes is arbitrary. However, for increasing λ the eigenvector \mathbf{e}_1 , i.e. the one corresponding to the largest eigenvalue of the RGT, aligns with \mathbf{n} . The other eigenvectors span the plane orthogonal to the preferred axis. To sum up, the density profiles originating from an anisotropic potential can be approximated by an ellipsoid using the RGT, whose major principle axis and aspect ratio are \mathbf{n} and λ . While these conclusions are summarized here only for one particular phase, this statement holds for

sufficiently high $\bar{\rho}$ for all three-dimensionally periodic density profiles which will be presented in the following sections of this chapter.

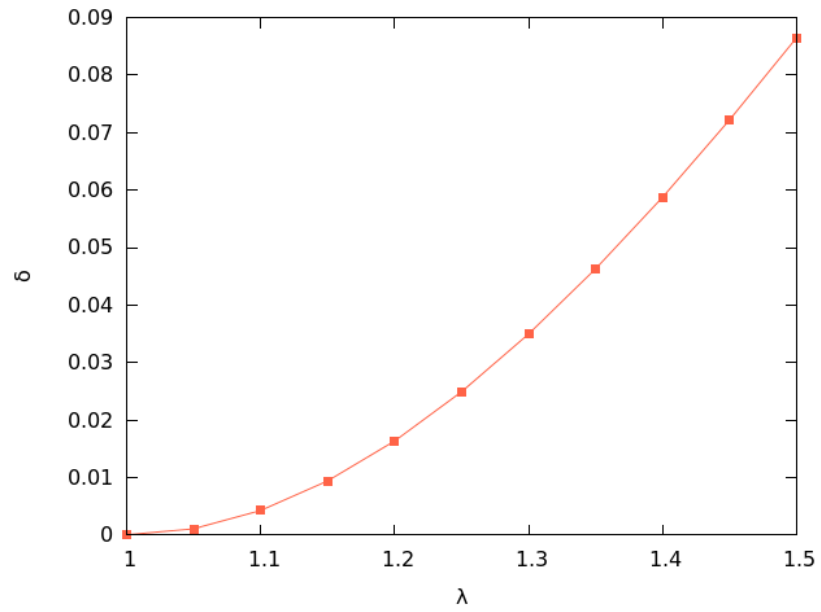


Figure 4.1: Asphericity δ of the density profile as a function of the anisotropy-parameter λ , for $T^* = 1.0$ and $\bar{\rho} = 7.0$.

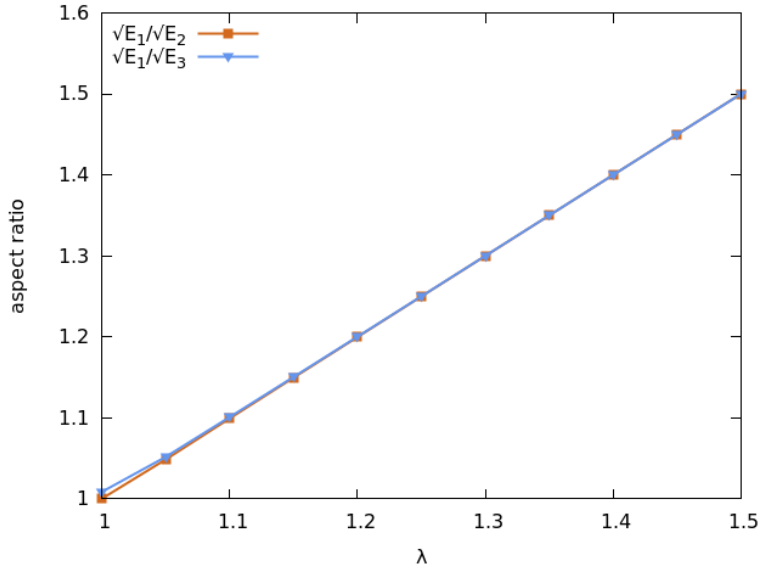


Figure 4.2: Aspect ratios $\sqrt{E_1/E_2}$ and $\sqrt{E_1/E_3}$ of the ellipsoid which approximates the density profile (via the RGT), as functions of the anisotropy-parameter λ , for $T^* = 1.0$ and $\bar{\rho} = 7.0$.

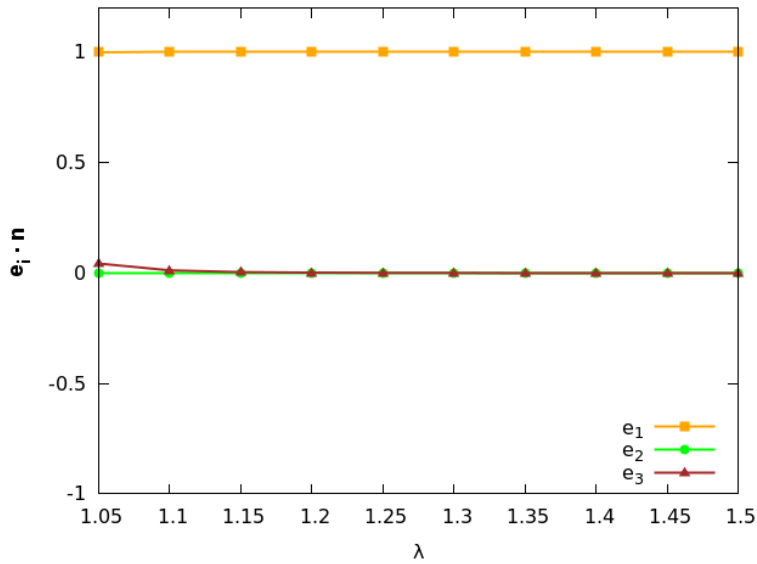


Figure 4.3: Scalar products of the principle axes of the ellipsoid approximating the density profile with the preferred axis \mathbf{n} (i.e.: $\mathbf{e}_1 \cdot \mathbf{n}$, $\mathbf{e}_2 \cdot \mathbf{n}$ and $\mathbf{e}_3 \cdot \mathbf{n}$) as functions of λ , for $T^* = 1.0$ and $\bar{\rho} = 7.0$.

The effects of the anisometry of the potential on the lattice vectors are not universal as they strongly depend on the chosen representation of the structure which serves as a starting point for the variation of λ . Therefore the results discussed in the following yield only a *qualitative* insight.

In Figs. 4.5,4.6 and 4.4 the lengths of the lattice vectors, their enclosed angles (α, β and γ ; see below) and their normed scalar products with the preferred axis \mathbf{n} are shown as functions of λ ; here, these scalar products are defined as $\mathbf{a}_i \cdot \mathbf{n}/|\mathbf{a}_i|$ which are thus equivalent to the cosine of the enclosed angles. The angles α, β and γ are defined as follows:

$$\alpha = \arccos \left(\frac{\mathbf{a}_1 \cdot \mathbf{a}_2}{|\mathbf{a}_1||\mathbf{a}_2|} \right) \quad (4.1.3)$$

$$\beta = \arccos \left(\frac{\mathbf{a}_1 \cdot \mathbf{a}_3}{|\mathbf{a}_1||\mathbf{a}_3|} \right) \quad (4.1.4)$$

$$\gamma = \arccos \left(\frac{\mathbf{a}_2 \cdot \mathbf{a}_3}{|\mathbf{a}_2||\mathbf{a}_3|} \right) \quad (4.1.5)$$

It can be observed that while the lengths of the lattice vectors and the angles enclosed are equal for $\lambda = 1.0$ this symmetry is broken for $\lambda > 1.0$. The impact of the anisometry of the potential on the lattice vectors depends on the orientation of the lattice vector with respect to \mathbf{n} : \mathbf{a}_1 and \mathbf{a}_3 , which enclose the same angle with \mathbf{n} for all λ (see Fig. 4.4), show similar behaviour of their lengths and orientations which differs from the behaviour of the length and orientation of \mathbf{a}_2 . The lengths of \mathbf{a}_1 and \mathbf{a}_3 are undistinguishable and show an increasing deviation from the length of \mathbf{a}_2 as λ is increased (see Fig. 4.5). Similarly, Fig. 4.6 shows that the dependence of α and γ (which both involve \mathbf{a}_2) on λ is different from the dependence of β (which does not involve \mathbf{a}_2) on λ .

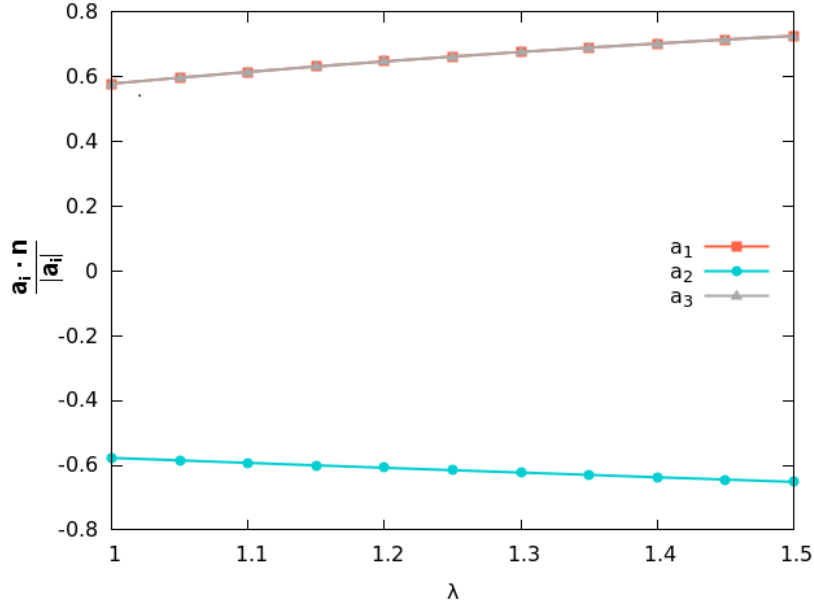


Figure 4.4: Normed scalar product $\mathbf{a}_i \cdot \mathbf{n}/|\mathbf{a}_i|$ as functions of λ , for $T^* = 1.0$ and $\bar{\rho} = 7.0$.

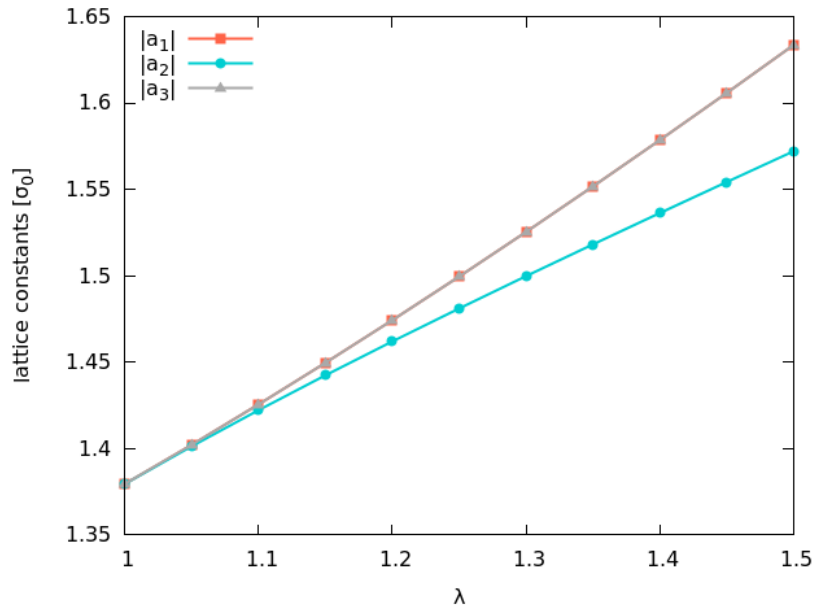


Figure 4.5: Length of the lattice vectors \mathbf{a}_i as functions of λ , for $T^* = 1.0$ and $\bar{\rho} = 7.0$.

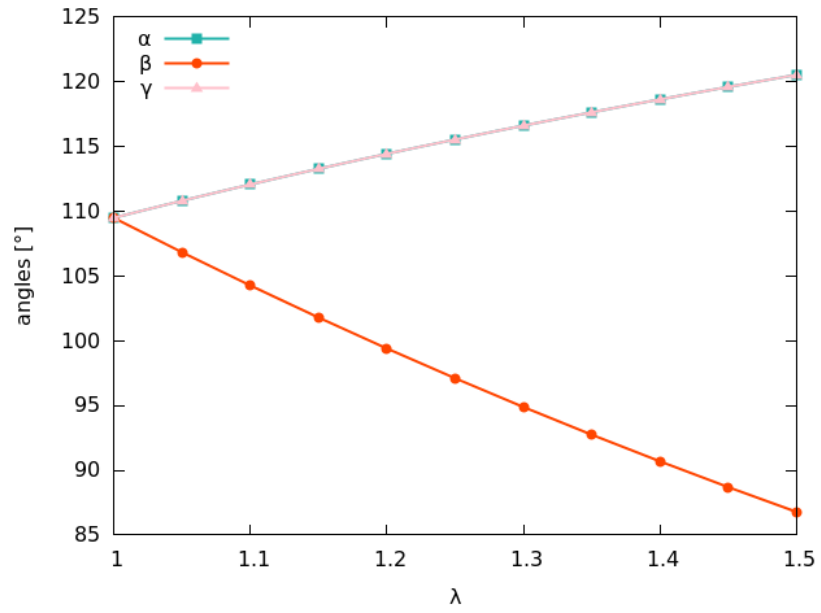


Figure 4.6: Angles α, β and γ (as defined in Eqs. (4.1.3), (4.1.4) and (4.1.5)) enclosed by the lattice vectors \mathbf{a}_i as functions of λ , for $T^* = 1.0$ and $\bar{\rho} = 7.0$.

4.2 Stable and Metastable Microphases of the modified GEM-4 Model

In contrast to the preceding section, where the impact of the anisotropy in the pair potential on the resulting density profile was studied, the goal is now to obtain information on the thermodynamic properties of the system. This might eventually lead to a phase diagram in the T^* - ρ^* -plane. Again a system where the particles interact via a modified GEM-4 potential with $\lambda = 1.5$ is considered.

The general outline to achieve this goal is to perform a global optimization of the density profile and of the lattice vectors at any state point in the T^* - ρ^* -plane within a region of interest. Therefore a search for *all* (at least the most stable) possible structures within a region of the T^* - ρ^* -plane of the phase diagram one is interested in is performed. Then the free energies of the identified structures for each state point (T^*, ρ^*) are compared in order to find the most stable structures. Lastly, it has to be checked whether two competing structures that have the same energy are equivalent.

For the first step, a large number of runs ($\gtrsim 700$) with randomly generated lattice parameters at randomly chosen state points within a specified region of the T^* - $\bar{\rho}\sigma_0^3$ -plane were performed. This region was chosen to be:

$$T^* \in [0, 1.1] \quad , \quad \bar{\rho}\sigma_0^3 \in [1, 8] \quad . \quad (4.2.1)$$

T^* and $\bar{\rho}\sigma_0^3$ were chosen such that T^* and ρ^* are located within the interval for which Pini et al. depicted a phase diagram for the spherical GEM-4 model in Ref. [11]. This choice is justified by the expectation that the system at hand is similar to the spherical GEM-4 system. Thus one might expect that the most stable phases of the model at hand are located within the same range of the T^* - ρ^* -plane. The lattice parameters were randomly generated as follows:

$$|\mathbf{a}_1|, |\mathbf{a}_2|, |\mathbf{a}_3| \in [0.5\sigma_0, 5.5\sigma_0] \quad , \quad \alpha, \beta, \gamma \in [40^\circ, 140^\circ] \quad . \quad (4.2.2)$$

The orientation of the vectors of the unit cell, defined by these parameters,

with respect to \mathbf{n} was chosen randomly as well.

The starting density profile was assumed to be a Gaussian for all runs which is given by

$$\rho_{\mathbf{n}} = \bar{\rho}\sigma_0^3 \exp \left[\left(\frac{\mathbf{x}_{\mathbf{n}}}{0.15\sigma_0} \right)^2 \right] . \quad (4.2.3)$$

Since the initial density has (according to the author's experience) little impact on the final result expression (4.2.3) is used as initial density instead of choosing this function randomly. This choice is justified *a posteriori* by the fact that despite the simple functional form in Eq. (4.2.3) a broad variety of density profiles can be obtained as emerging density profiles. Of course, it is not guaranteed that the minimization always converges. In fact, about 25% of the runs lead to convergence (for a detailed discussion of the convergence criterion see Appendix A).

In the following overview over the obtained structures they are classified according to the periodicity of the respective density profile:

- (a) **homogeneous density (liquid)**
- (b) **1D-periodic (lamellar) density profile:** homogeneous in two spatial directions
- (c) **2D-periodic (rod-like) density profile:** homogeneous in one spatial direction
- (d) **3D-periodic (cluster crystal) density profile:** periodic with respect to three linearly independent vectors (\mathbf{a}_1 , \mathbf{a}_2 , \mathbf{a}_3)

Generic examples for three types of structures ((b),(c) and (d)) are shown in Figs. 4.7, 4.8 and 4.9.

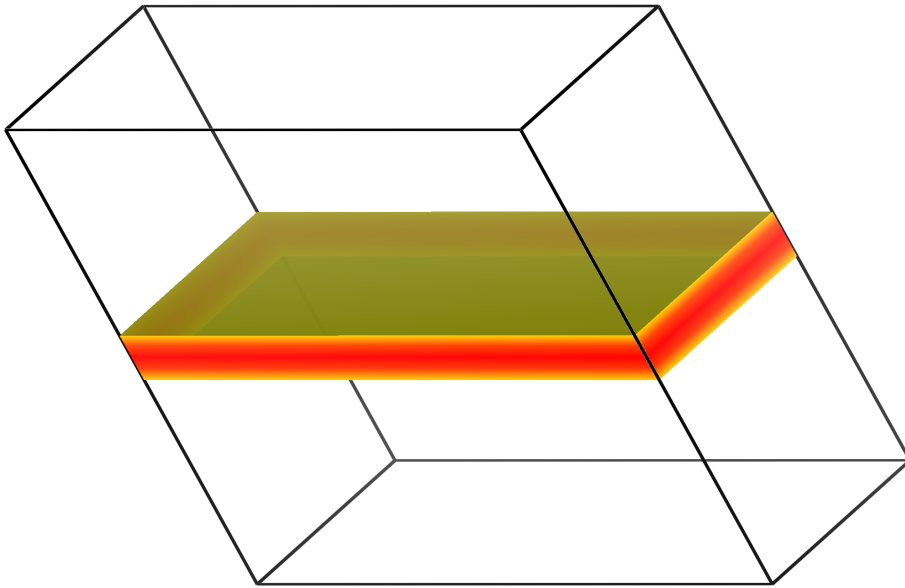


Figure 4.7: Generic example for a 1D-periodic density profile where spatial variations are only observed in one direction. The yellow layers at the top and at the bottom of the correspond to isosurfaces with constant density. The red section in between indicates that the density within the yellow layers is higher than the one at the isosurfaces.

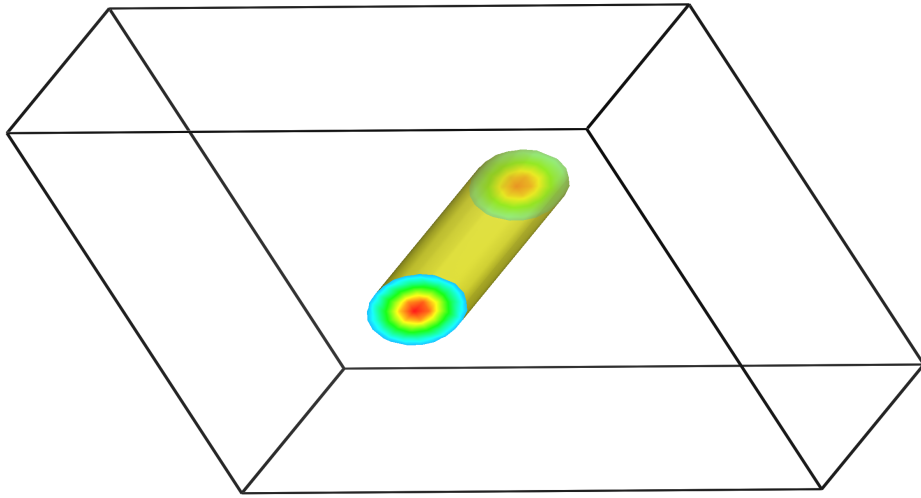


Figure 4.8: Generic example for a 2D-periodic density profile where spatial variations are observed in two directions. The yellow layer corresponds to an isosurface with constant density. The colours ranging from blue to red indicate the density profile of the cross-section of the structure.

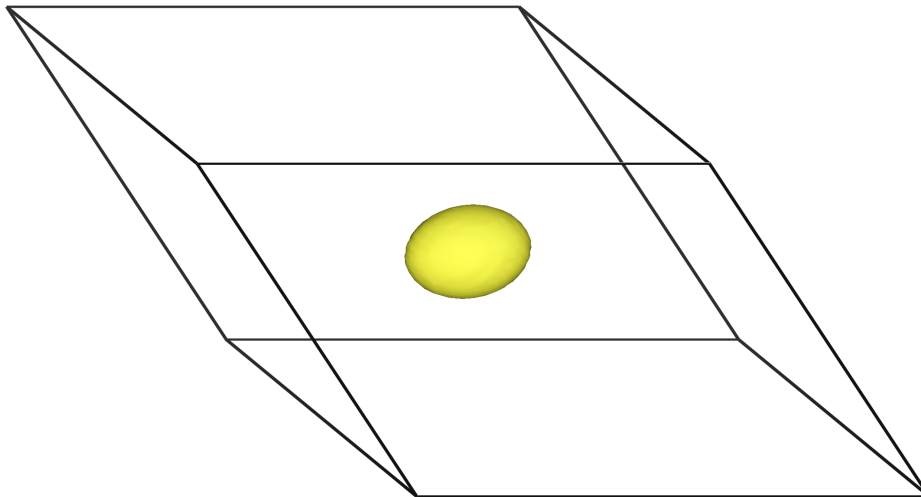


Figure 4.9: Generic example for a 3D-periodic structure where spatial variations are observed in three directions. The yellow surface corresponds to an isosurface with constant density.

As a first step in distinguishing between metastable and stable phases, the

free energies of these classes of structures were compared within the region of the phase diagram specified in Eq. (4.2.1).

It was found that 1D- and 2D-periodic structures only occur as metastable phases, as there are no regions in the T^* - ρ^* -plane where they yield the lowest free energy. This is exemplified by Figs. 4.10 and 4.11 where the reduced free energy densities $\beta F \sigma_0^3 / V$ of the four classes of structures are shown as functions of the density ρ^* with fixed values of T^* . Fig. 4.11 exhibits a phase transition between a liquid and an ordered (3D) phase.

A closer look at this phase transition is taken in Fig. 4.12: here, the free energies of the homogeneous and the 3D-periodic structures are shown around the crossing of the two curves for fixed $T^* = 1.0$. One can determine the coexistence region for the liquid and the ordered phase by constructing a double-tangent. This is typically the way to construct the phase diagram but this has not been done within this thesis. However by determining the value of ρ^* where the curves of the free energies cross for several values of T^* one can at least create an estimate of the phase diagram in the T^* - ρ^* -plane. This estimate is shown in Fig. 4.13: the dashed line separates the region of a stable liquid and a periodic structure and is obtained by determining the state points where the free energies of the liquid and the ordered structure cross. A detailed quantitative analysis of the phase transition would have passed the limits of this thesis. Instead, emphasis was put on investigating the periodic structures, which will be discussed in the following.

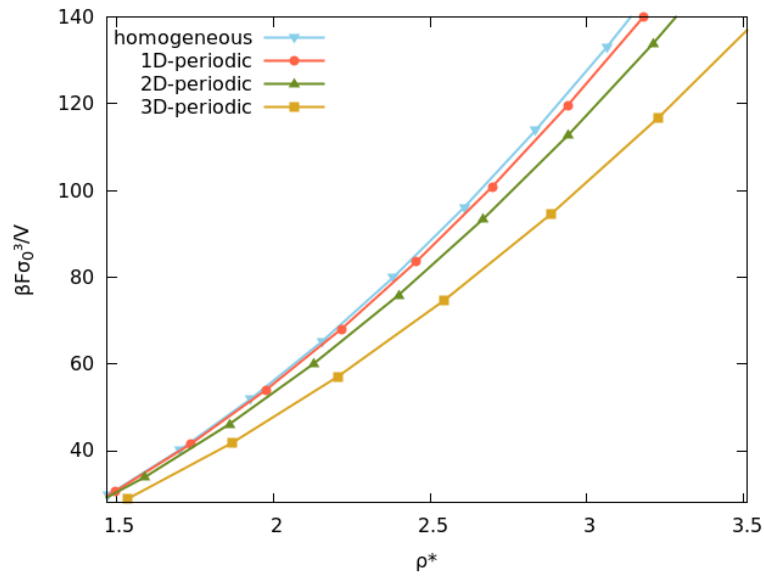


Figure 4.10: Reduced free energy density $\beta F \sigma_0^3 / V$ as a function of the reduced density ρ^* for the four classes of density profiles specified in the text at fixed reduced temperature $T^* = 0.2$.

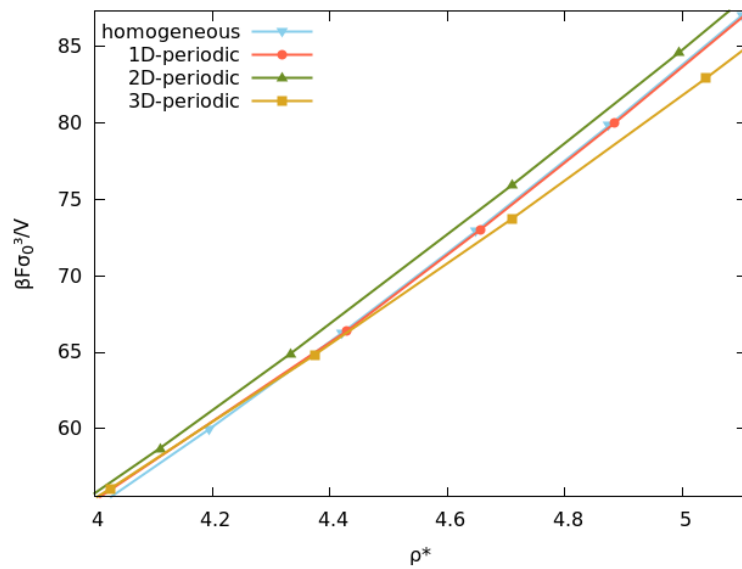


Figure 4.11: Reduced free energy density $\beta F \sigma_0^3 / V$ as a function of the reduced density ρ^* for the four classes of density profiles specified in the text at fixed reduced temperature $T^* = 1.0$.

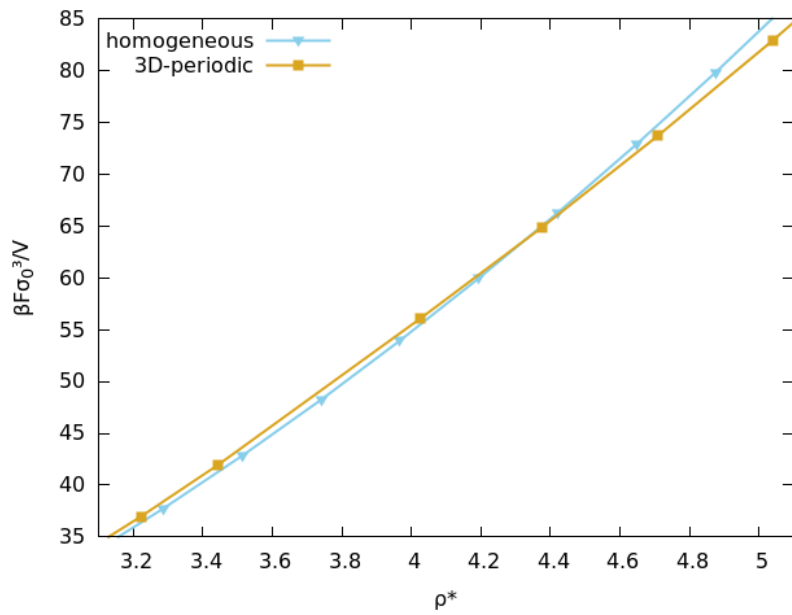


Figure 4.12: Reduced free energy density $\beta F \sigma_0^3 / V$ as a function of the reduced density near the phase transition from liquid to an ordered structure at fixed reduced temperature $T^* = 1.0$.

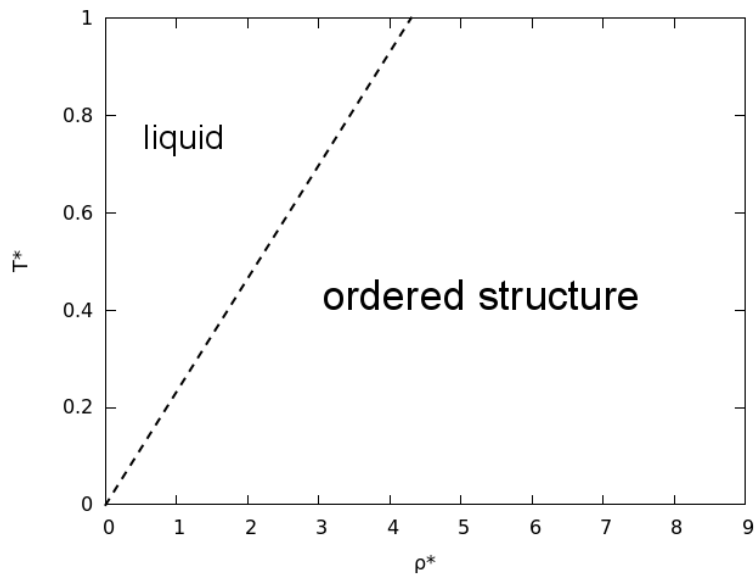


Figure 4.13: Sketch of the phase diagram of a system interacting via a modified GEM-4 potential with $\lambda = 1.5$ in the T^* - ρ^* -plane.

4.3 Cluster Crystals Formed by a Modified GEM-4 Model

In the preceding section it was shown that there is a large region of the phase diagram where 3D-periodic phases yield the lowest energy. In the following a detailed analysis of the density profiles and of the free energies of the respective structures within this region is presented.

Among all the optimization runs, where the starting parameters are chosen as specified in Sec. 4.2, 127 converged to a 3D-periodic lattice. A detailed analysis has been done for *all* of these structures but for the sake of simplicity *eight* phases (out of 127) are selected and analysed in the following. Note that all the occurring phenomena discussed below (scattering of the quantities for low densities and regrouping of the energies into two groups) are present within *all* structures found within this thesis.

In general (and as specified below) it can be observed that for values of ρ^* that are close to the minimal density for which an inhomogeneous phase can be found the quantities characterizing the shape (R_g , δ , ζ and $\sqrt{E_1/E_2}$) and the orientation (\mathbf{e}_1 , \mathbf{e}_2 and \mathbf{e}_3) of the density profile scatter. This feature vanishes as ρ^* is increased and these quantities show the same dependence on ρ^* for all 3D-periodic structures.

The dependence of the radius of gyration R_g on ρ^* is shown in Fig. 4.14: it can be observed that with increasing ρ^* the density profile becomes more and more localized (this feature is also found in the spherical GEM-4 Model [11]). The asphericity δ (Fig. 4.15) converges to 0.0865 which is in accordance with the result discussed in Sec. 4.1 (see Fig. 4.1). The acylindricity ζ (Fig. 4.16) is non-vanishing for low ρ^* but rapidly goes to 0 for higher ρ^* . The aspect-ratio of the ellipsoid that approximates the density profile ($\sqrt{E_1/E_2}$) converges to λ for sufficiently high ρ^* (note that $\sqrt{E_1/E_2} = \sqrt{E_1/E_3}$ for vanishing ζ)

The dependence of the orientation of the principle-axes of that ellipsoid on ρ^* is shown in Fig. 4.18, 4.19 and 4.20. The principle-axis corresponding to the highest eigenvalue \mathbf{e}_1 coincides with the preferred axis \mathbf{n} and the other

principle-axes \mathbf{e}_2 and \mathbf{e}_3 span the plane orthogonal to \mathbf{n} for sufficiently high ρ^* .

To sum up, it was found that all the quantities characterizing the shape and the orientation show some scattering for low ρ^* but the same behaviour as ρ^* is increased.

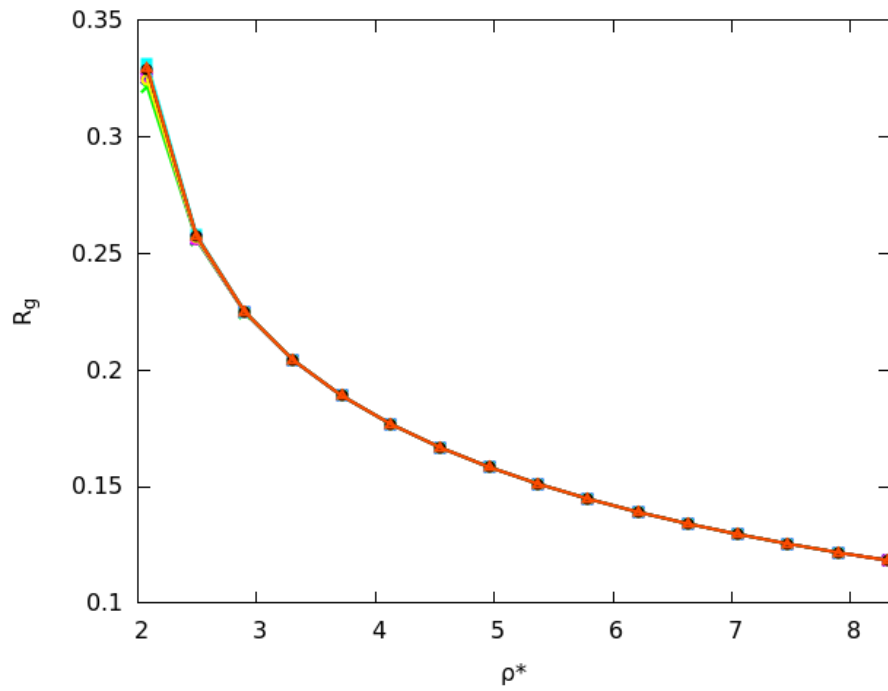


Figure 4.14: Radius of gyration R_g as a function of the reduced density ρ^* for the modified GEM-4 model with $\lambda = 1.5$ at fixed reduced temperature $T^* = 0.5$.

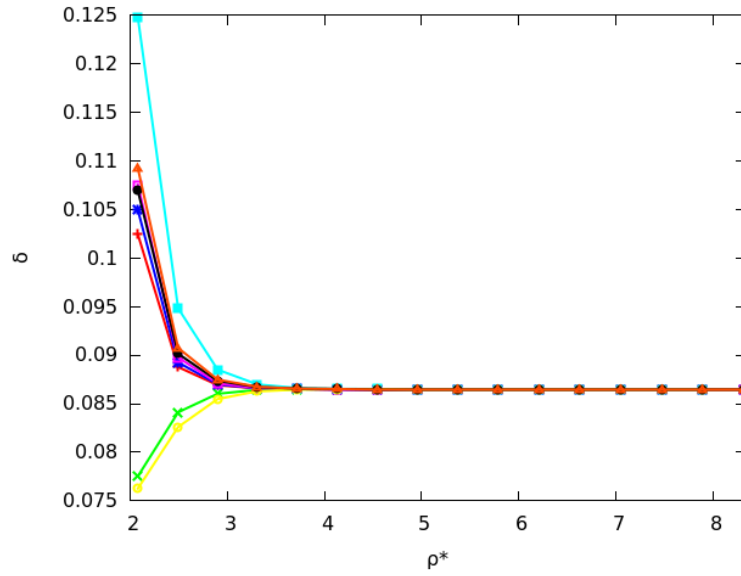


Figure 4.15: Asphericity δ as a function of the reduced density ρ^* for the modified GEM-4 model with $\lambda = 1.5$ at fixed reduced temperature $T^* = 0.5$.

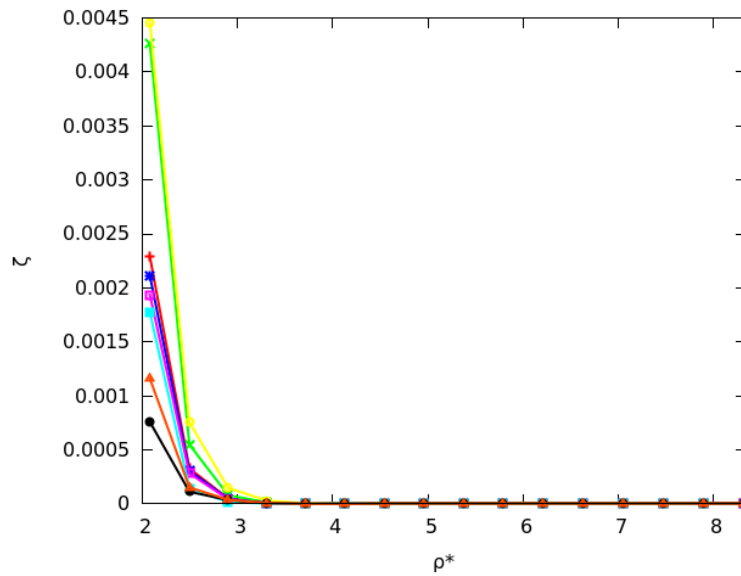


Figure 4.16: Acylindricity ζ as a function of the reduced density ρ^* for the modified GEM-4 model with $\lambda = 1.5$ at fixed reduced temperature $T^* = 0.5$.

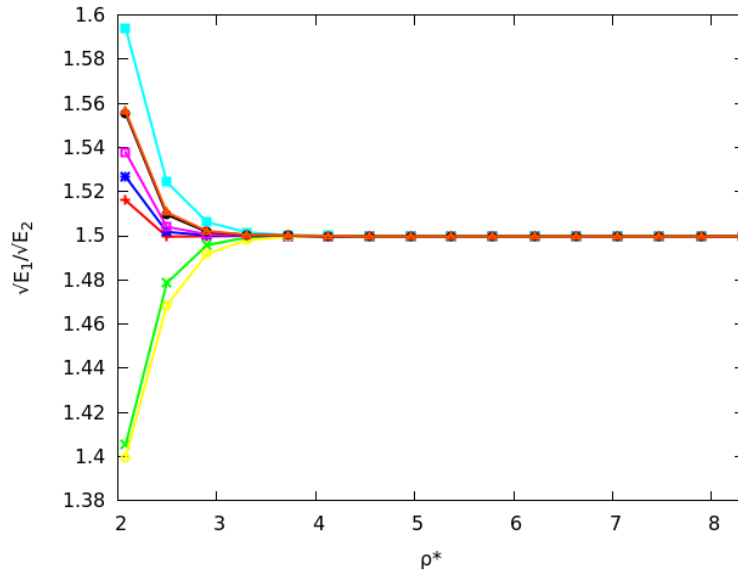


Figure 4.17: Aspect ratio $\sqrt{E_1/E_2}$ of the ellipsoid which approximates the density profile as a function of the reduced density ρ^* for the modified GEM-4 model with $\lambda = 1.5$ at fixed reduced temperature $T^* = 0.5$.

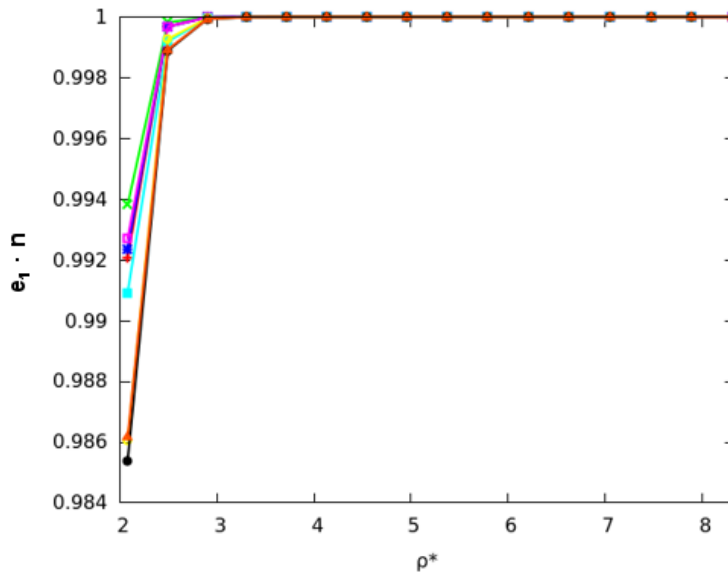


Figure 4.18: Scalar product of the principle-axis corresponding to the highest eigenvalue with the preferred axis $\mathbf{e}_1 \cdot \mathbf{n}$ as a function of the reduced density ρ^* for the modified GEM-4 model with $\lambda = 1.5$ at fixed reduced temperature $T^* = 0.5$.

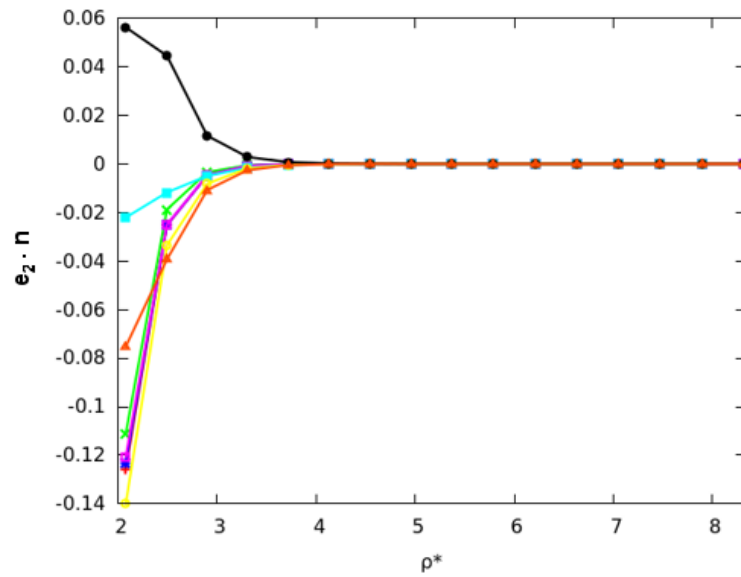


Figure 4.19: Scalar product of the principle-axis corresponding to the second highest eigenvalue with the preferred axis $\mathbf{e}_2 \cdot \mathbf{n}$ as a function of the reduced density ρ^* for the modified GEM-4 model with $\lambda = 1.5$ at fixed reduced temperature $T^* = 0.5$.

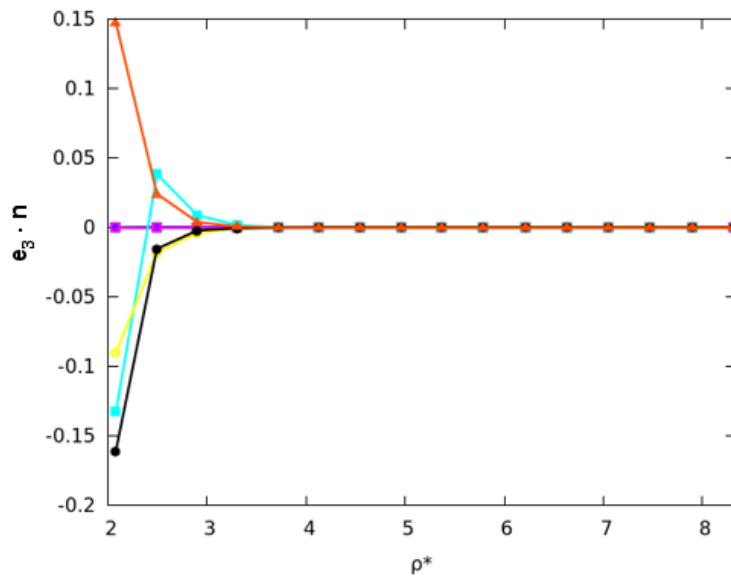


Figure 4.20: Scalar product of the principle-axis corresponding to the lowest eigenvalue with the preferred axis $\mathbf{e}_3 \cdot \mathbf{n}$ as a function of the reduced density ρ^* for the modified GEM-4 model with $\lambda = 1.5$ at fixed reduced temperature $T^* = 0.5$.

In the following, the respective reduced free energy densities $\beta F \sigma_0^3 / V$ of the eight structures are discussed in detail. The different values of $\beta F \sigma_0^3 / V$ show again scattering for low ρ^* values; however, unlike the structural quantities discussed above, convergence to *two* distinct values can be observed (Fig. 4.21). Thus the eight ordered structures can be regrouped in two sets. The gap between the respective values of the reduced free energy densities is of the order of 10^{-5} ; further the scattering of the values of the reduced free energy densities within each of the groups is of the order of 10^{-9} which represents essentially the limit of the numerical accuracy of the algorithm [69]. A similar regrouping of the eight structures into the two sets of lattices is also observed at the level of the reduced ideal free energy density $\beta F_{\text{id}} \sigma_0^3 / V$ and the reduced excess free energy density $\beta F_{\text{ex}} \sigma_0^3 / V$ (see Figs. 4.22 and 4.22).

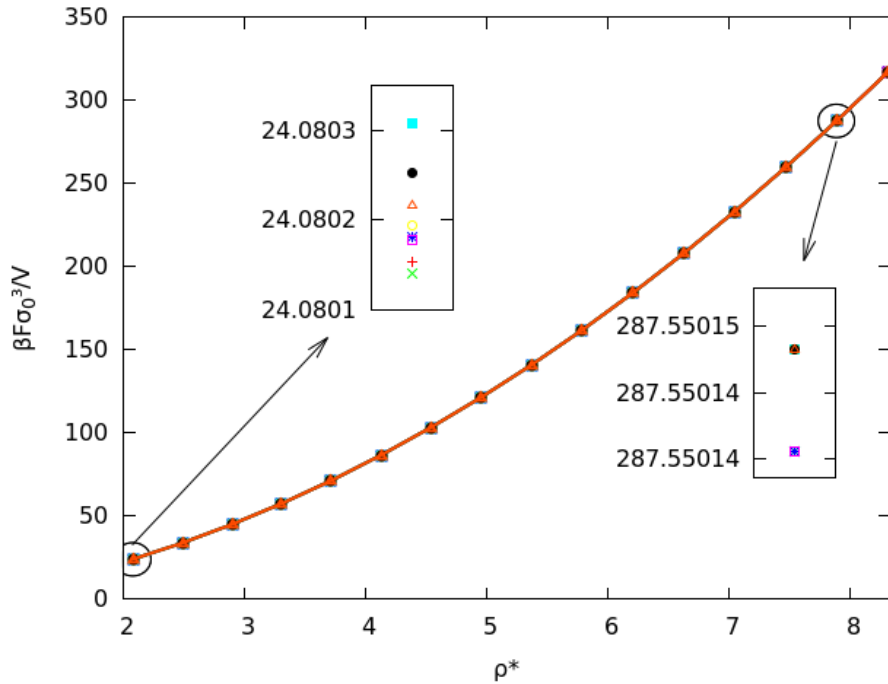


Figure 4.21: Reduced free energy density $\beta F \sigma_0^3 / V$ for the modified GEM-4 model as a function of ρ^* for fixed reduced temperature $T^* = 0.5$. The insets show an enlarged view of the reduced free energy densities for two selected values of ρ^* .

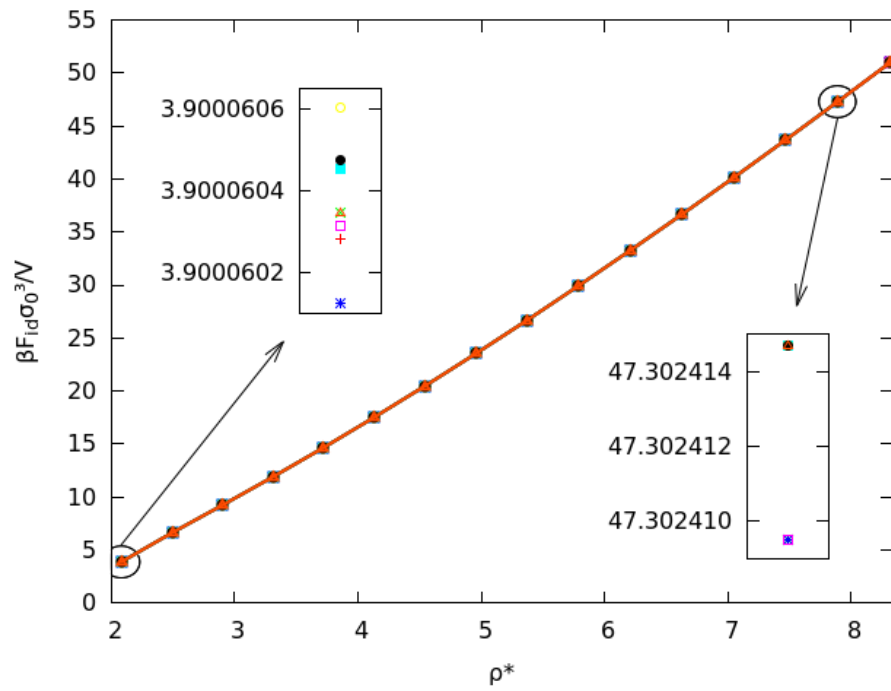


Figure 4.22: Reduced ideal free energy density $\beta F_{id} \sigma_0^3 / V$ for the modified GEM-4 model as a function of ρ^* for fixed reduced temperature $T^* = 0.5$. The insets show an enlarged view of the reduced free energy densities for two selected values of ρ^* .

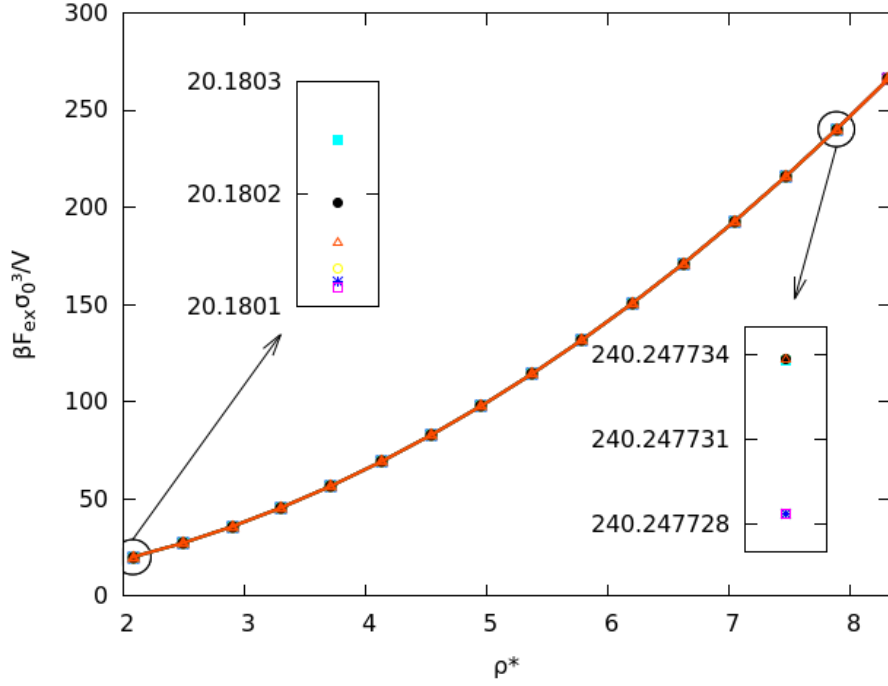


Figure 4.23: Reduced excess free energy density $\beta F_{\text{ex}} \sigma_0^3 / V$ for the modified GEM-4 model as a function of ρ^* for fixed reduced temperature $T^* = 0.5$. The insets show an enlarged view of the reduced free energy densities for two selected values of ρ^* .

The fact that differences of the respective reduced free energy densities within each of the groups of structures differ by a value that hits the limit of numerical accuracy is a strong indication that all structures pertaining to a group are equivalent. Of course, that this does not necessarily mean that the respective vectors $(\mathbf{a}_1, \mathbf{a}_2, \mathbf{a}_3)$ that specify the unit cell of those structures are equal, as in general the characterisation of a unit cell of a certain lattice in terms of the lattice vectors is not unique [63].

In the following, the question, whether the structures within the group of lattices with the lowest reduced free energy density (I-IV) are equivalent and whether the structures within the group with the higher reduced free energy density (V-VIII) are equivalent, is further explored. The lattice vectors defining the primitive cells (the unit cells containing only a single lattice point) of the structures I-VIII for $\rho^* = 7.894$, $T^* = 0.5$ and $\mathbf{n} = (1, 0, 0)$ are given

by (in units of σ_0)

	\mathbf{a}_1	\mathbf{a}_2	\mathbf{a}_3
I	$\begin{pmatrix} 2.1029 \\ -0.0329 \\ 0.1952 \end{pmatrix}$	$\begin{pmatrix} -1.0150 \\ 1.2419 \\ -0.0656 \end{pmatrix}$	$\begin{pmatrix} 0.8237 \\ 0.3653 \\ 1.2528 \end{pmatrix}$
II	$\begin{pmatrix} 1.7780 \\ 0.6505 \\ 0.4174 \end{pmatrix}$	$\begin{pmatrix} 0.2156 \\ 1.3956 \\ -0.1845 \end{pmatrix}$	$\begin{pmatrix} -0.2532 \\ -0.5279 \\ 1.3020 \end{pmatrix}$
III	$\begin{pmatrix} 2.0155 \\ -0.3704 \\ 0.2447 \end{pmatrix}$	$\begin{pmatrix} -0.5889 \\ 1.3547 \\ 0.1144 \end{pmatrix}$	$\begin{pmatrix} 0.7738 \\ 0.0383 \\ 1.3171 \end{pmatrix}$
IV	$\begin{pmatrix} 2.0212 \\ 0.3885 \\ -0.1921 \end{pmatrix}$	$\begin{pmatrix} 0.5309 \\ 1.3699 \\ 0.0385 \end{pmatrix}$	$\begin{pmatrix} -0.8926 \\ 0.1178 \\ 1.2789 \end{pmatrix}$
V	$\begin{pmatrix} 2.0346 \\ 0.0248 \\ 0.4037 \end{pmatrix}$	$\begin{pmatrix} -1.0356 \\ 1.2129 \\ -0.2361 \end{pmatrix}$	$\begin{pmatrix} 0.5284 \\ -0.3683 \\ 1.3205 \end{pmatrix}$
VI	$\begin{pmatrix} 1.6787 \\ 0.8596 \\ 0.1100 \end{pmatrix}$	$\begin{pmatrix} -0.2757 \\ 1.4034 \\ 0.0092 \end{pmatrix}$	$\begin{pmatrix} -0.6140 \\ -0.7747 \\ 1.1117 \end{pmatrix}$
VII	$\begin{pmatrix} 2.0704 \\ -0.0053 \\ 0.3134 \end{pmatrix}$	$\begin{pmatrix} -1.0101 \\ 1.2272 \\ -0.2097 \end{pmatrix}$	$\begin{pmatrix} 0.6437 \\ -0.3586 \\ 1.300 \end{pmatrix}$
VIII	$\begin{pmatrix} 2.1070 \\ 0.1463 \\ -0.0944 \end{pmatrix}$	$\begin{pmatrix} 0.8472 \\ 1.2780 \\ -0.2263 \end{pmatrix}$	$\begin{pmatrix} -0.8973 \\ -0.2985 \\ 1.2476 \end{pmatrix}$

If two primitive cells are equivalent it is necessary that their respective volumes match (see for instance [63]). Indeed, Fig. 4.24 shows that the volume of the primitive cells of structures I-IV and V-VIII attain two distinct values for high ρ^* , where the differences of these values within one group range at the limit of numerical accuracy. The difference between the values for v of the two groups is of the order of 10^{-8} .

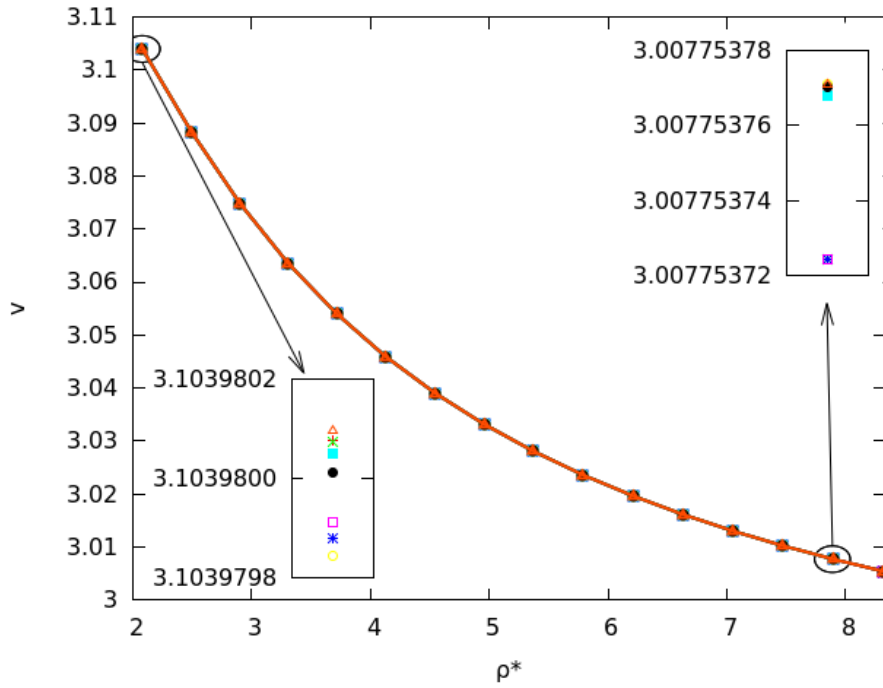


Figure 4.24: Volume of the unit cell v as a function of ρ^* for fixed reduced temperature ($T^* = 0.5$). The insets show an enlarged view of the volume of the unit cell for two selected values of ρ^* . The grouping of the values in two distinct groups is obvious.

However, a detailed analysis of the primitive cells shows that they are in fact *not* equivalent. One way to prove this is by choosing a random lattice site and taking a look at its nearest-neighbours (NN). If two lattices are equivalent the numbers of the nearest-neighbours, the second-nearest-neighbours, etc. and their corresponding distances have to be equal. The NN-distances can be determined by using VESTA (see Fig. 4.25 and 4.26). It was found that the NN-distances are different even within each group of structures:

	Number of NN	NN-distance [σ_0]
I	2	1.3267
II	2	1.4245
III	2	1.4395
IV	2	1.4697
V	2	1.2965
VI	2	1.4303
VII	2	1.3098
VIII	2	1.3787

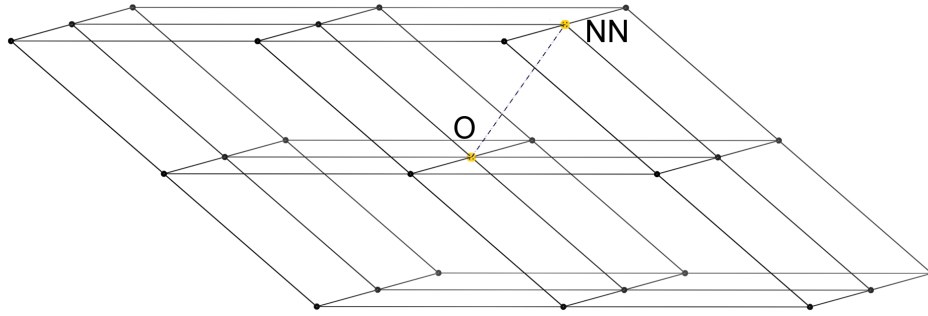


Figure 4.25: Sketch of the lattice of structure I. NN denotes the nearest-neighbour to the lattice site at the origin O. The corresponding NN-distance (dashed line) is $1.3267\sigma_0$.

The fact that different structures yield undistinguishable free energies is remarkable and the question whether this is a genuine effect or only present at the current level of accuracy is still under investigation.

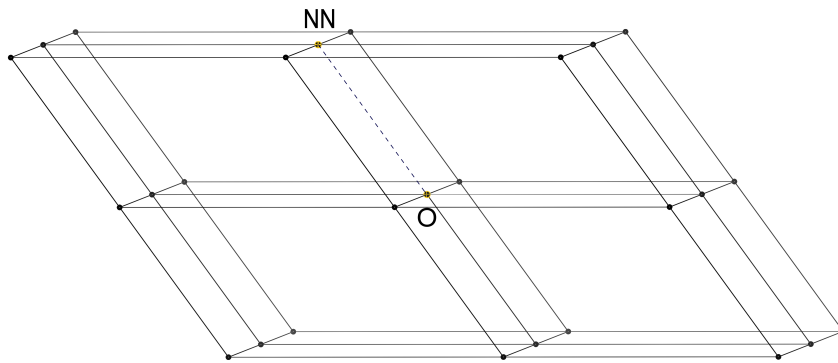


Figure 4.26: Sketch of the lattice of structure II. NN denotes the nearest-neighbour to the lattice site at the origin O. The corresponding NN-distance (dashed line) is $1.4245\sigma_0$.

Chapter 5

Conclusion & Outlook

Results presented in this thesis have provided unambiguous evidence that anisotropy in the inter-particle potential has a substantial impact on the formation of ordered structures in soft matter systems. This impact has been shown quantitatively for a simple model for ultrasoft particles, where the main axes of the particles are assumed to be oriented in one single direction. The calculations were performed within the framework of classical density functional theory using a simple, mean-field-like form for the excess free energy.

Even for this simple model the deviations in the density profile from sphericity are significant. It was shown that the shape and the orientation of the interaction are reflected by the shape and the orientation of the single-particle density. Furthermore it was found that the differences in the free energies between two competing structures are at the limit of numerical accuracy. A yet open question is whether this feature is a genuine effect or if it is only present within the current limit of accuracy.

The unconstrained minimization algorithm applied to the functional within this thesis may be cumbersome to implement and numerically expensive but has proven to be feasible and worthwhile, as it imposes no *a priori* assumptions on the density profile. Thus it can be applied to a huge variety of systems and can easily be extended to more than one species of particles.

This thesis' subject constitutes a first step towards the description of the formation of ordered structure formed by ultrasoft, anisometric particles. In order to obtain a deeper insight into this topic, future explorations will include

- proceeding to particles with distinct orientations
- an investigation of more sophisticated ultrasoft interactions (e.g. potentials where the interaction strength depends on the inter-particle vector and the orientation of the particles)

both allowing for a more realistic description of ultrasoft, anisometric particles.

Appendix A

Details of the Minimization Algorithm

The minimization algorithm is based on preceding work of Pini et al. [11]. The functional $\Omega(\rho_{\mathbf{n}}, \mathbf{b}_i)$ (see Eq. (3.2.9)) is minimized with respect to the $\rho_{\mathbf{n}}$ by a preconditioned conjugate-gradient algorithm with adaptive step size (see Appendix A.1). The minimization algorithm of $\Omega(\rho_{\mathbf{n}}, \mathbf{b}_i)$ with respect to the vectors \mathbf{b}_i of the reciprocal lattice is a basic steepest descent with adaptive step size (see Appendix A.2).

The minimization of the functional is performed until the quantity

$$N^3 \sum_{\mathbf{n}} \partial(\beta\Omega/V)/\partial\rho_{\mathbf{n}} + \sum_{i,j} \partial(\beta\Omega/V)/\partial B_{ij} \quad (\text{A.0.1})$$

becomes smaller than 10^{-15} , where B_{ij} denotes the entries of a matrix \mathbf{B} obtained by arranging the \mathbf{b}_i into columns:

$$\mathbf{B} = (\mathbf{b}_1, \mathbf{b}_2, \mathbf{b}_3) \quad . \quad (\text{A.0.2})$$

A.1 Minimizing the functional with respect to the density profile

In the following, k will denote the iteration index of the minimization of the functional. As a first step for every iteration, the quantity $\xi_{\mathbf{n}}^k$ is calculated

via the following preconditioner:

$$\xi_{\mathbf{n}}^k = \frac{\partial(\beta\Omega/V)}{\partial\rho_{\mathbf{n}}^k} \left(\frac{\partial^2(\beta\Omega/V)}{\partial(\rho_{\mathbf{n}}^k)^2} \right)^{-1} . \quad (\text{A.1.1})$$

The purpose of using the Jacobi preconditioner is to make long plain regions in the energy surface less elongated [11]. Secondly the "downhill" direction $\psi_{\mathbf{n}}^k$ (see below) is calculated via the conjugate gradient method, i.e. $\psi_{\mathbf{n}}^k$ a linear combination of $\xi_{\mathbf{n}}^k$ and the direction of the previous step $\psi_{\mathbf{n}}^{k-1}$ as defined in [65]:

$$\psi_{\mathbf{n}}^k = \xi_{\mathbf{n}}^k + \zeta^k \psi_{\mathbf{n}}^{k-1} \quad (\text{A.1.2})$$

$$\zeta^k = \frac{\sum_{\mathbf{n}} \xi_{\mathbf{n}}^k (\xi_{\mathbf{n}}^k - \xi_{\mathbf{n}}^{k-1})}{\sum_{\mathbf{n}} (\xi_{\mathbf{n}}^{k-1})^2} . \quad (\text{A.1.3})$$

The $\rho_{\mathbf{n}}$ are updated after each iteration step via

$$\rho_{\mathbf{n}}^{k+1} = \rho_{\mathbf{n}}^k - \eta^k \psi_{\mathbf{n}}^k \quad (\text{A.1.4})$$

where η^k denotes the step size (discussion below) of the k -th iteration. The $\rho_{\mathbf{n}}^{k+1}$ must be non-negative as they represent the single-particle densities. However this feature is not automatically guaranteed by Eq. (A.1.4). Hence, $\rho_{\mathbf{n}}^{k+1}$ is set to a small positive number (10^{-20}) whenever Eq. (A.1.4) leads to a negative result. The optimal choice for the step size η^k is determined by minimizing $g^k(\eta) = \beta\Omega(\rho_{\mathbf{n}}^k - \eta\psi_{\mathbf{n}}^k; B_{ij})/V$ with respect to η for fixed $\rho_{\mathbf{n}}^k$, $\psi_{\mathbf{n}}^k$ and B_{ij} . Following Pini et al. [11] this is realized by solving

$$\left. \frac{\partial g^k}{\partial \eta} \right|_{\eta=\eta^k} = 0 \quad (\text{A.1.5})$$

via the Newton-Raphson method (see, for instance [64]). As found by Pini et al., the step size η^k is calculated via a *single* Newton-Raphson step, given by

$$\eta^k = - \left. \frac{\partial g^k}{\partial \eta} \left(\frac{\partial^2 g^k}{\partial \eta^2} \right)^{-1} \right|_{\eta=0} . \quad (\text{A.1.6})$$

As the functional (3.2.9) is not globally convex the expression above could also lead to a negative step size [11]. Whenever this happens, η^k is set to a

small positive value instead (10^{-3}). The first and second derivatives in Eq. (A.1.1) and Eq. (A.1.6) are given by

$$\frac{\partial(\beta\Omega/V)}{\partial\rho_{\mathbf{n}}} = \frac{1}{N^3}[\ln(\rho_{\mathbf{n}}/\bar{\rho}) - \beta\mu_{ex}] + \frac{\beta}{N^6} \sum_{\mathbf{m}} e^{-2\pi i\mathbf{m}\cdot\mathbf{n}/N} \hat{\rho}_{\mathbf{m}} \tilde{v}(\mathbf{q}_{\mathbf{m}}) \quad (\text{A.1.7})$$

$$\frac{\partial^2(\beta\Omega/V)}{\partial(\rho_{\mathbf{n}})^2} = \frac{1}{N^3} \frac{1}{\rho_{\mathbf{n}}} + \frac{\beta}{N^6} \sum_{\mathbf{m}} \tilde{v}(\mathbf{q}_{\mathbf{m}}) \quad (\text{A.1.8})$$

$$\frac{\partial g}{\partial\eta} = - \sum_{\mathbf{n}} \frac{\partial(\beta\Omega/V)}{\partial\rho_{\mathbf{n}}} \psi_{\mathbf{n}} \quad (\text{A.1.9})$$

$$\frac{\partial^2 g}{\partial\eta^2} = \frac{1}{N^3} \sum_{\mathbf{n}} \frac{1}{\rho_{\mathbf{n}}} (\psi_{\mathbf{n}})^2 + \frac{\beta}{N^6} \sum_{\mathbf{m}} \tilde{v}(\mathbf{q}_{\mathbf{m}}) \hat{\psi}_{\mathbf{m}} \hat{\psi}_{-\mathbf{m}} \quad (\text{A.1.10})$$

A.2 Minimizing with respect to the lattice parameters

The minimization of the grand potential functional (Eq. (3.2.9)) with respect to the lattice parameters B_{ij} is performed via a basic steepest descent algorithm with adaptive step size. The "downhill" direction ψ_{ij}^k in step k is straightforwardly given by the gradient, thus

$$\psi_{ij}^k = \frac{\partial(\beta\Omega/V)}{\partial B_{ij}^k} \quad (\text{A.2.1})$$

$$B_{ij}^{k+1} = B_{ij}^k - \alpha^k \psi_{ij}^k \quad (\text{A.2.2})$$

The optimal step size α^k is given by minimizing $h^k(\alpha) = \beta\Omega(\rho_{\mathbf{n}}; B_{ij}^k - \alpha\psi_{ij}^k)/V$ for fixed $\rho_{\mathbf{n}}$, B_{ij}^k and ψ_{ij}^k . The step size parameter for the k -th iteration α^k is calculated via a single Newton-Raphson step:

$$\alpha^k = - \frac{\partial h^k}{\partial\alpha} \left(\frac{\partial^2 h^k}{\partial\alpha^2} \right)^{-1} \Bigg|_{\alpha=0} \quad (\text{A.2.3})$$

As discussed above this expression could also result in a negative α^k . Analogous to η^k it is then set to a small positive number (10^{-3}). The gradient in

Eq. (A.2.1) and the derivatives in Eq. (A.2.3) are given by

$$\frac{\partial(\beta\Omega/V)}{\partial B_{ij}} = \frac{\beta}{2N^6} \sum_{\mathbf{m}} \hat{\rho}_{\mathbf{m}} \hat{\rho}_{-\mathbf{m}} \frac{\partial \tilde{v}(\mathbf{q}_{\mathbf{m}})}{\partial q_j} m_i \quad (\text{A.2.4})$$

$$\frac{\partial h}{\partial \alpha} = - \sum_{ij} \left(\frac{\partial(\beta\Omega/V)}{\partial B_{ij}} \right)^2 \quad (\text{A.2.5})$$

$$\frac{\partial^2 h}{\partial \alpha^2} = \sum_{ij,kl} \frac{\partial^2(\beta\Omega/V)}{\partial B_{ij} \partial B_{kl}} \frac{\partial(\beta\Omega/V)}{\partial B_{ij}} \frac{\partial(\beta\Omega/V)}{\partial B_{kl}} \quad (\text{A.2.6})$$

$$\frac{\partial^2(\beta\Omega/V)}{\partial B_{ij} \partial B_{kl}} = \frac{\beta}{2N^6} \sum_{\mathbf{m}} \hat{\rho}_{\mathbf{m}} \hat{\rho}_{-\mathbf{m}} \frac{\partial^2 \tilde{v}(\mathbf{q}_{\mathbf{m}})}{\partial q_i \partial q_j} m_k m_l \quad (\text{A.2.7})$$

The differential $\partial/\partial q_i$ denotes differentiation with respect to the i -th component of an vector \mathbf{q} of the reciprocal space. The gradient and the Hessian of the Fourier transform of the pair potential $\tilde{v}(\mathbf{q})$ can either be calculated by numerical differentiation or, as done here, by Fourier transforming suitably defined functions: the gradient can be written as

$$\frac{\partial \tilde{v}(\mathbf{q})}{\partial q_i} = i \int d\mathbf{r} e^{-i\mathbf{q}\cdot\mathbf{r}} [r_i v(\mathbf{r})] \quad (\text{A.2.8})$$

and in an analogous manner, the Hessian can be written as

$$\frac{\partial^2 \tilde{v}(\mathbf{q})}{\partial q_i \partial q_j} = - \int d\mathbf{r} e^{-i\mathbf{q}\cdot\mathbf{r}} [r_i r_j v(\mathbf{r})] \quad (\text{A.2.9})$$

where r_i denotes the i -th component of the position vector \mathbf{r} . The integrals in Eq. (A.2.8) and (A.2.9) can be evaluated using the FFTW-package by approximating the integrals by a sum.

Note that in the calculation of the respective step sizes η^k (Eq. (A.1.6)) and α^k (Eq. (A.2.3)) the dependence on the other variable is neglected: performing the complete Newton-Raphson method in order to calculate η^k and α^k includes simultaneously solving the equations $\partial f^k(\eta, \alpha)/\partial \eta = 0$ and $\partial f^k(\eta, \alpha)/\partial \alpha = 0$ where $f^k = \beta\Omega(\rho_{\mathbf{n}} - \eta\psi_{\mathbf{n}}^k; B_{ij}^k - \alpha\psi_{ij}^k)/V$. A single Newton-Raphson step is given by

$$\eta^k = \left(-\frac{\partial^2 f^k}{\partial \alpha^2} \frac{\partial f^k}{\partial \eta} + \frac{\partial^2 f^k}{\partial \alpha \partial \eta} \frac{\partial f^k}{\partial \alpha} \right) \left(\frac{\partial^2 f^k}{\partial \eta^2} \frac{\partial^2 f^k}{\partial \alpha^2} - \left(\frac{\partial^2 f^k}{\partial \alpha \partial \eta} \right)^2 \right)^{-1} \Bigg|_{\alpha, \eta=0} \quad (\text{A.2.10})$$

$$\alpha^k = \left(-\frac{\partial^2 f^k}{\partial \eta^2} \frac{\partial f^k}{\partial \alpha} + \frac{\partial^2 f^k}{\partial \alpha \partial \eta} \frac{\partial f^k}{\partial \eta} \right) \left(\frac{\partial^2 f^k}{\partial \eta^2} \frac{\partial^2 f^k}{\partial \alpha^2} - \left(\frac{\partial^2 f^k}{\partial \alpha \partial \eta} \right)^2 \right)^{-1} \Bigg|_{\alpha, \eta=0} \quad (\text{A.2.11})$$

which reduce to Eq. (A.1.6) and Eq. (A.2.3) when disregarding the terms $\partial^2 f^k / (\partial \alpha \partial \eta)$. Doing so is in principle less efficient but found to be more robust [11].

Appendix B

Summation over the Reciprocal Lattice

When calculating the grand potential for a single-particle density profile via the grand potential functional (3.2.9) and when performing the optimization algorithm as explained in Appendix A, one needs to perform summations over the lattice points of the reciprocal lattice (denoted by \mathbf{m}). As the reciprocal lattice consists of infinitely many lattice sites this cannot be done exactly. Within this thesis, the following approximation is made:

$$\sum_{\mathbf{m}}(\dots) \approx \sum_{\mathbf{m}, |m_i| \leq M} (\dots) \quad (\text{B.0.1})$$

The summation over all $\mathbf{m} = (m_1, m_2, m_3)$ with $m_i \in \mathbb{Z}$ is replaced by a summation where all the terms with $|m_i| > M$ are neglected, where M is a suitably chosen parameter (see below). This is a reasonable approximation as the summands in Eq. (3.2.9) and Appendix A involve either the Fourier transform $\tilde{v}(\mathbf{q}_{\mathbf{m}})$, its gradient $\partial\tilde{v}/\partial q_j(\mathbf{q}_{\mathbf{m}})$ or the Hessian $\partial^2\tilde{v}/(\partial q_i\partial q_j)(\mathbf{q}_{\mathbf{m}})$ which become negligibly small for large \mathbf{q} (see Fig. 2.5). Of course, the appropriate choice of M depends on the type of pair potential which is considered. Fig. B.1 shows the dependence of the free energy on M for the anisotropic GEM-4 potential ($\lambda = 1.5$) considered within this thesis. In Fig. B.2 the difference of the free energies of two competing phases for $\lambda = 1.5$ is shown. This energy difference is of the order of 10^{-5} , which is not an unusual

order of magnitude for the energy difference between stable and metastable phases [69]. Note that the energy difference changes its sign when increasing M from 3 to 4. Therefore $M = 3$ would lead to a wrong prediction on the stable phase.

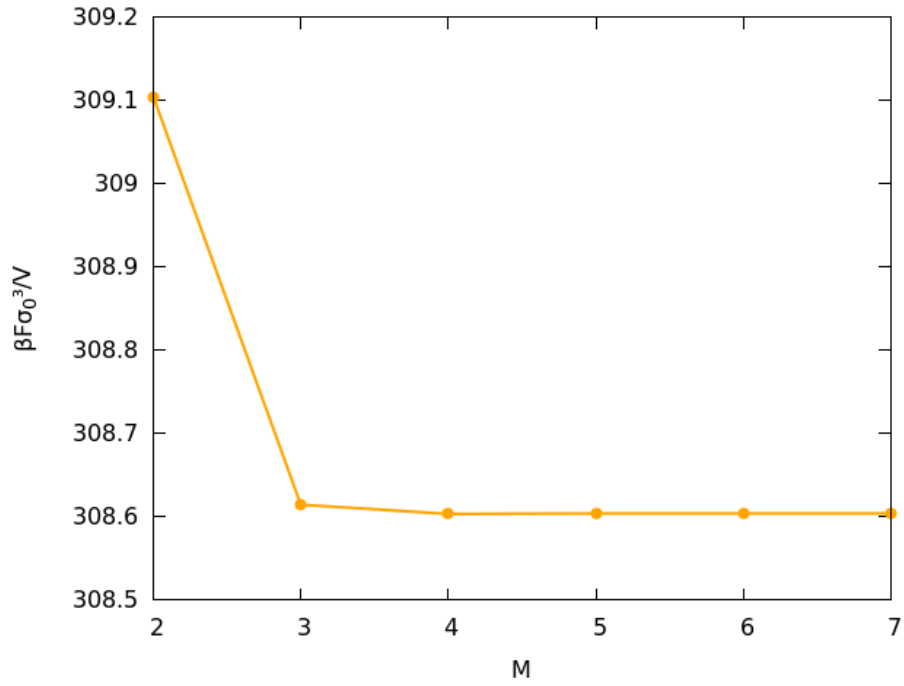


Figure B.1: Dependence of $\beta F \sigma_0^3 / V$ on the cut-off value M for $\lambda = 1.5$ of a structure which is a member of the group yielding the lower energy (see Sec. 4.3).

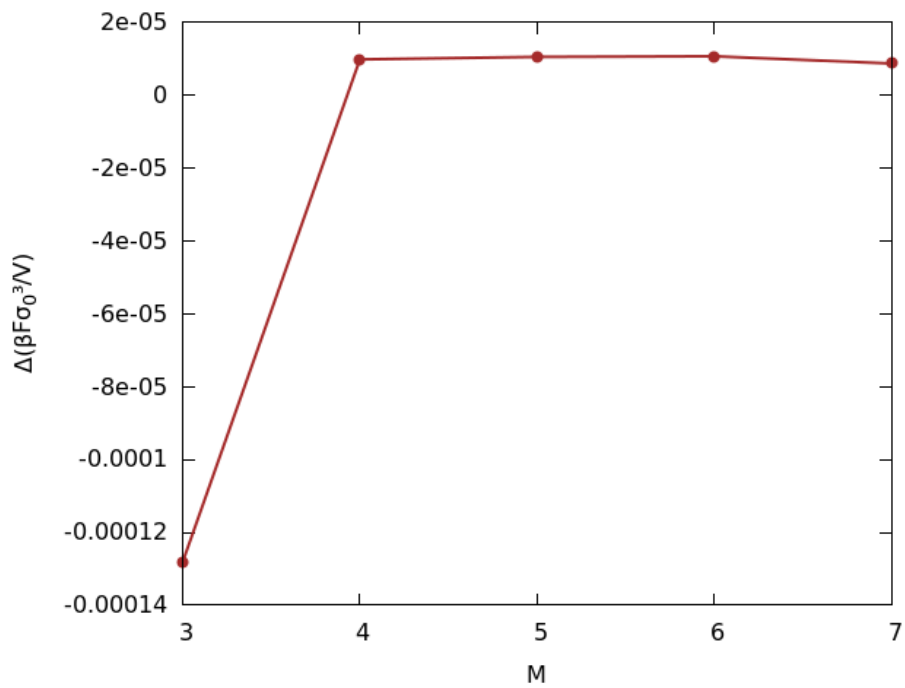


Figure B.2: Dependence of the difference between the free energies on the cut-off value M of the two groups of structures (see Sec. 4.3) of a system interacting via an anisometric pair potential with $\lambda = 1.5$. While this difference is negative for $M = 3$ it is positive for $M \geq 4$.

Bibliography

- [1] R. P. Sear and W. M. Gelbart, “Microphase separation versus the vapor-liquid transition in systems of spherical particles,” *The Journal of Chemical Physics*, vol. 110, no. 9, pp. 4582–4588, 1999.
- [2] F. Sciortino, S. Mossa, E. Zaccarelli, and P. Tartaglia, “Equilibrium cluster phases and low-density arrested disordered states: The role of short-range attraction and long-range repulsion,” *Physical Review Letters*, vol. 93, p. 055701, Jul 2004.
- [3] S. Mossa, F. Sciortino, P. Tartaglia, and E. Zaccarelli, “Ground-state clusters for short-range attractive and long-range repulsive potentials,” *Langmuir*, vol. 20, no. 24, pp. 10756–10763, 2004. PMID: 15544413.
- [4] A. I. Campbell, V. J. Anderson, J. S. van Duijneveldt, and P. Bartlett, “Dynamical arrest in attractive colloids: The effect of long-range repulsion,” *Physical Review Letters*, vol. 94, p. 208301, May 2005.
- [5] R. Sanchez and P. Bartlett, “Equilibrium cluster formation and gelation,” *Journal of Physics: Condensed Matter*, vol. 17, no. 45, p. S3551, 2005.
- [6] A. Imperio and L. Reatto, “A bidimensional fluid system with competing interactions: spontaneous and induced pattern formation,” *Journal of Physics: Condensed Matter*, vol. 16, no. 38, p. S3769, 2004.
- [7] A. Imperio and L. Reatto, “Microphase separation in two-dimensional systems with competing interactions,” *The Journal of Chemical Physics*, vol. 124, no. 16, p. 164712, 2006.

- [8] C. N. Likos, C. Mayer, E. Stiakakis, and G. Petekidis, “Clustering of soft colloids due to polymer additives,” *Journal of Physics: Condensed Matter*, vol. 17, no. 45, p. S3363, 2005.
- [9] E. Stiakakis, G. Petekidis, D. Vlassopoulos, C. N. Likos, H. Iatrou, N. Hadjichristidis, and J. Roovers, “Depletion and cluster formation in soft colloid - polymer mixtures,” *EPL (Europhysics Letters)*, vol. 72, no. 4, p. 664, 2005.
- [10] P. Charbonneau and D. R. Reichman, “Systematic characterization of thermodynamic and dynamical phase behavior in systems with short-ranged attraction,” *Physical Review E*, vol. 75, p. 011507, Jan 2007.
- [11] D. Pini, A. Parola, and L. Reatto, “An unconstrained dft approach to microphase formation and application to binary gaussian mixtures,” *The Journal of Chemical Physics*, vol. 143, no. 3, p. 034902, 2015.
- [12] A. J. Archer, C. N. Likos, and R. Evans, “Soft-core binary fluid exhibiting a lambda-line and freezing to a highly delocalized crystal,” *Journal of Physics: Condensed Matter*, vol. 16, no. 23, p. 297, 2004.
- [13] A. J. Archer, “Density functional theory for the freezing of soft-core fluids,” *Physical Review E*, vol. 72, no. 5, p. 051501, 2005.
- [14] C. N. Likos, B. M. Mladek, D. Gottwald, and G. Kahl, “Why do ultrasoft repulsive particles cluster and crystallize? analytical results from density functional theory,” *The Journal of Chemical Physics* 126, 224502 (2007), 2007.
- [15] B. M. Mladek, D. Gottwald, G. Kahl, M. Neumann, and C. N. Likos, “Formation of polymorphic cluster phases for a class of models of purely repulsive soft spheres,” *Physical Review Letters*, vol. 96, p. 045701, Jan 2006.
- [16] S. Prestipino, F. Saija, and P. V. Giaquinta, “Phase diagram of the gaussian-core model,” *Physical Review E*, vol. 71, p. 050102, May 2005.

- [17] G. Gompper, M. Schick, and S. Milner, “Self-Assembling Amphiphilic Systems,” *Physics Today*, vol. 48, p. 91, 1995.
- [18] C. N. Likos, “Effective interactions in soft condensed matter physics,” *Physics Reports*, vol. 348, no. 4, pp. 267–439, 2001.
- [19] B. Kruger, L. Schäfer, and A. Baumgärtner, “Correlations among interpenetrating polymer coils : the probing of a fractal,” *Journal de Physique France*, vol. 50, no. 21, pp. 3191–3222, 1989.
- [20] J. Dautenhahn and C. K. Hall, “Monte carlo simulation of off-lattice polymer chains: effective pair potentials in dilute solution,” *Macromolecules*, vol. 27, no. 19, pp. 5399–5412, 1994.
- [21] A. A. Louis, P. G. Bolhuis, J. P. Hansen, and E. J. Meijer, “Can polymer coils be modeled as “soft colloids”?,” *Physical Review Letters*, vol. 85, pp. 2522–2525, Sep 2000.
- [22] I. O. Götze, H. M. Harreis, and C. N. Likos, “Tunable effective interactions between dendritic macromolecules,” *The Journal of Chemical Physics*, vol. 120, no. 16, pp. 7761–7771, 2004.
- [23] M. Ballauff and C. N. Likos, “Dendrimers in solution: insight from theory and simulation,” *Angewandte Chemie International Edition*, vol. 43, no. 23, pp. 2998–3020, 2004.
- [24] A. R. Denton, “Erratum: Counterion penetration and effective electrostatic interactions in solutions of polyelectrolyte stars and microgels,” *Physical Review E*, vol. 68, no. 4, p. 049904, 2003.
- [25] D. Gottwald, C. N. Likos, G. Kahl, and H. Löwen, “Ionic microgels as model systems for colloids with an ultrasoft electrosteric repulsion: Structure and thermodynamics,” *The Journal of Chemical Physics*, vol. 122, no. 7, p. 074903, 2005.
- [26] D. Gottwald, C. N. Likos, G. Kahl, and H. Löwen, “Phase behavior of ionic microgels,” *Physical Review Letters*, vol. 92, no. 6, p. 068301, 2004.

- [27] C. Pierleoni, C. Addison, J. P. Hansen, and V. Krakoviack, “Multiscale coarse graining of diblock copolymer self-assembly: From monomers to ordered micelles,” *Physical Review Letters*, vol. 96, no. 12, p. 128302, 2006.
- [28] J. P. Hansen and C. Pearson, “Athermal models for diblock copolymer self-assembly,” *Molecular Physics*, vol. 104, no. 22-24, pp. 3389–3397, 2006.
- [29] C. N. Likos, A. Lang, M. Watzlawek, and H. Löwen, “Criterion for determining clustering versus reentrant melting behavior for bounded interaction potentials,” *Physical Review E*, vol. 63, p. 031206, Feb 2001.
- [30] C. Z. Mooney, *Monte carlo simulation*, vol. 116. Sage Publications, 1997.
- [31] J. Haile, *Molecular dynamics simulation*, vol. 18. Wiley, New York, 1992.
- [32] R. Evans, “The nature of the liquid-vapour interface and other topics in the statistical mechanics of non-uniform, classical fluids,” *Advances in Physics*, vol. 28, no. 2, pp. 143–200, 1979.
- [33] S. Sacanna, D. J. Pine, and G. R. Yi, “Engineering shape: the novel geometries of colloidal self-assembly,” *Soft Matter*, vol. 9, pp. 8096–8106, 2013.
- [34] S. M. Yang, S. H. Kim, J. M. Lim, and G. R. Yi, “Synthesis and assembly of structured colloidal particles,” *Journal of Materials Chemistry*, vol. 18, no. 19, pp. 2177–2190, 2008.
- [35] L. Onsager, “The effects of shape on the interaction of colloidal particles,” *Annals of the New York Academy of Sciences*, vol. 51, no. 1, pp. 627–659, 1949.
- [36] P. A. Buining, A. P. Philipse, and H. N. W. Lekkerkerker, “Phase behavior of aqueous dispersions of colloidal boehmite rods,” *Langmuir*, vol. 10, no. 7, pp. 2106–2114, 1994.

- [37] D. Frenkel and B. M. Mulder, “The hard ellipsoid-of-revolution fluid: I. monte carlo simulations,” *Molecular physics*, vol. 55, no. 5, pp. 1171–1192, 1985.
- [38] B. Götzelmann, R. Evans, and S. Dietrich, “Depletion forces in fluids,” *Phys. Rev. E*, vol. 57, pp. 6785–6800, Jun 1998.
- [39] S. Asakura and F. Oosawa, “On interaction between two bodies immersed in a solution of macromolecules,” *The Journal of Chemical Physics*, vol. 22, no. 7, pp. 1255–1256, 1954.
- [40] L. Rossi, S. Sacanna, W. T. M. Irvine, P. M. Chaikin, D. J. Pine, and A. P. Philipse, “Cubic crystals from cubic colloids,” *Soft Matter*, vol. 7, no. 9, pp. 4139–4142, 2011.
- [41] S. Sacanna, W. Irvine, L. Rossi, and D. J. Pine, “Lock and key colloids through polymerization-induced buckling of monodisperse silicon oil droplets,” *Soft Matter*, vol. 7, no. 5, pp. 1631–1634, 2011.
- [42] Q. Chen, J. Yan, J. Zhang, S. C. Bae, and S. Granick, “Janus and multiblock colloidal particles,” *Langmuir*, vol. 28, no. 38, pp. 13555–13561, 2012.
- [43] Q. Chen, S. C. Bae, and S. Granick, “Directed self-assembly of a colloidal kagome lattice,” *Nature*, no. 469, pp. 381–384, 2011.
- [44] K. Chaudhary, Q. Chen, J. J. Juarez, S. Granick, and J. A. Lewis, “Janus colloidal matchsticks,” *Journal of the American Chemical Society*, vol. 134, no. 31, pp. 12901–12903, 2012.
- [45] G. Kahl and H. Löwen, “Classical density functional theory: an ideal tool to study heterogeneous crystal nucleation,” *Journal of Physics: Condensed Matter*, vol. 21, no. 46, p. 464101, 2009.
- [46] J. P. Hansen and I. R. McDonald, *Theory of Simple Liquids*. Academic Press, 2006.

- [47] L. Ornstein and F. Zernike, “The influence of accidental deviations of density on the equation of state,” *Koninklijke Nederlandsche Akademie van Wetenschappen Proceedings*, vol. 19, no. 2, pp. 1312–1315, 1914.
- [48] A. R. Denton and N. W. Ashcroft, “Density-functional approach to the structure of classical uniform fluids,” *Physical Review A*, vol. 44, pp. 1219–1227, Jul 1991.
- [49] A. R. Denton and N. W. Ashcroft, “High-order direct correlation functions of uniform classical liquids,” *Physical Review A*, vol. 39, pp. 426–429, Jan 1989.
- [50] J. L. Barrat, J. P. Hansen, and G. Pastore, “Factorization of the triplet direct correlation function in dense fluids,” *Physical Review Letters*, vol. 58, pp. 2075–2078, May 1987.
- [51] D. Ruelle, *Statistical Mechanics*. WSPC/ICP, 1999.
- [52] F. H. Stillinger and D. K. Stillinger, “Negative thermal expansion in the gaussian core model,” *Physica A: Statistical Mechanics and its Applications*, vol. 244, no. 1, pp. 358 – 369, 1997.
- [53] A. Lang, C. N. Likos, M. Watzlawek, and H. Löwen, “Fluid and solid phases of the gaussian core model,” *Journal of Physics: Condensed Matter*, vol. 12, no. 24, p. 5087, 2000.
- [54] P. V. Giaquinta and F. Saija, “Re-entrant melting in the gaussian-core model: The entropy imprint,” *ChemPhysChem*, vol. 6, no. 9, pp. 1768–1771, 2005.
- [55] S. Prestipino, F. Saija, and P. V. Giaquinta, “Phase diagram of softly repulsive systems: The gaussian and inverse-power-law potentials,” *The Journal of Chemical Physics*, vol. 123, no. 14, p. 144110, 2005.
- [56] C. Senfter. private communication.

- [57] A. Ghoufi, D. Morineau, R. Lefort, and P. Malfreyt, “Configurational temperature and local properties of the anisotropic gay–berne liquid crystal model: Applications to the isotropic liquid/vapor interface and isotropic/nematic transition,” *The Journal of Chemical Physics*, vol. 134, no. 3, p. 034116, 2011.
- [58] R. S. Stein and J. M. Powers, *Topics in Polymer Physics*. Imperial College Press, 2006.
- [59] I. Georgiou, *Simulations of Soft Matter Systems*. Dissertation, Technical University of Vienna, 2014.
- [60] K. Šolc, “Shape of a random-flight chain,” *The Journal of Chemical Physics*, vol. 55, no. 1, pp. 335–344, 1971.
- [61] A. I. Kostrikin and Y. I. Manin, *Linear Algebra and Geometry*. Gordon and Breach Science Publishers, 1997.
- [62] J. Rudnick and G. Gaspari, “The asphery of random walks,” *Journal of Physics A: Mathematical and General*, vol. 19, no. 4, p. L191, 1986.
- [63] N. W. Ashcroft and D. N. Mermin, *Festkörperphysik*. Oldenbourg Wissenschaftsverlag GmbH, 2013.
- [64] W. H. Press, S. A. Teukolsky, W. T. Vetterling, and B. P. Flannery, *Numerical Recipes*. Cambridge University Press, 2007.
- [65] E. Polak and G. Ribiere, “Note sur la convergence de méthodes de directions conjuguées,” *Revue française d’informatique et de recherche opérationnelle. Série rouge*, vol. 3, no. 16, pp. 35–43, 1969.
- [66] M. Frigo and S. G. Johnson, “The design and implementation of fftw3,” *Proceedings of the IEEE*, vol. 93, pp. 216–231, Feb 2005.
- [67] L. Dagum and R. Menon, “Openmp: an industry standard api for shared-memory programming,” *IEEE computational science and engineering*, vol. 5, no. 1, pp. 46–55, 1998.

[68] www.vsc.ac.at.

[69] D. Pini. private communication.